

The *XMM* Cluster Survey: Forecasting cosmological and cluster scaling-relation parameter constraints

Martin Sahlén,^{1*} Pedro T. P. Viana,^{2,3} Andrew R. Liddle,¹ A. Kathy Romer,¹ Michael Davidson,⁴ Mark Hosmer,¹ Ed Lloyd-Davies,¹ Kivanc Sabirli,⁵ Chris A. Collins,⁶ Peter E. Freeman,⁵ Matt Hilton,^{7,8} Ben Hoyle,⁹ Scott T. Kay,¹⁰ Robert G. Mann,⁴ Nicola Mehrkens,¹ Christopher J. Miller,¹¹ Robert C. Nichol,⁹ S. Adam Stanford^{12,13} and Michael J. West^{14,15} (The XCS Collaboration)[†]

¹*Astronomy Centre, University of Sussex, Falmer, Brighton BN1 9QH, UK*

²*Departamento de Matemática Aplicada da Faculdade de Ciências da Universidade do Porto, Rua do Campo Alegre, 687, 4169-007 Porto, Portugal*

³*Centro de Astrofísica da Universidade do Porto, Rua das Estrelas, 4150-762 Porto, Portugal*

⁴*SUPA, Institute for Astronomy, University of Edinburgh, Blackford Hill, Edinburgh, EH9 9HJ, UK*

⁵*Department of Physics, Carnegie Mellon University, 5000 Forbes Avenue, Pittsburgh, PA-15217, USA*

⁶*Astrophysics Research Institute, Liverpool John Moores University, Twelve Quays House, Egerton Wharf, Birkenhead CH41 1LD, UK*

⁷*Astrophysics & Cosmology Research Unit, School of Mathematical Sciences, University of KwaZulu–Natal, Private Bag X54001, Durban 4000, S. Africa*

⁸*South African Astronomical Observatory, PO Box 9, Observatory, 7935, Cape Town, S. Africa*

⁹*ICG, University of Portsmouth, Portsmouth PO1 2EG, UK*

¹⁰*Jodrell Bank Centre for Astrophysics, School of Physics and Astronomy, The University of Manchester, Manchester M13 9PL, UK*

¹¹*Cerro-Tololo Inter-American Observatory, National Optical Astronomy Observatory, 950 North Cherry Avenue, Tucson, AZ 85719, USA*

¹²*Department of Physics, University of California at Davis, 1 Shields Avenue, Davis, CA 95616-8677, USA*

¹³*Institute of Geophysics & Planetary Physics, Lawrence Livermore National Laboratory, L-413, P.O. Box 808, 7000 E. Avenue, Livermore, CA 94551, USA*

¹⁴*Gemini Observatory, Casilla 603, La Serena, Chile*

¹⁵*European Southern Observatory, Alonso de Córdova 3107, Vitacura, Casilla 19001, Santiago 19, Chile*

26 April 2009

ABSTRACT

We forecast the constraints on the values of σ_8 , Ω_m , and cluster scaling relation parameters which we expect to obtain from the *XMM* Cluster Survey (XCS). We assume a flat Λ CDM Universe and perform a Monte Carlo Markov Chain analysis of the evolution of the number density of galaxy clusters that takes into account a detailed simulated selection function. Comparing our current observed number of clusters shows good agreement with predictions. We determine the expected degradation of the constraints as a result of self-calibrating the luminosity–temperature relation (with scatter), including temperature measurement errors, and relying on photometric methods for the estimation of galaxy cluster redshifts. We examine the effects of systematic errors in scaling relation and measurement error assumptions. Using only (T, z) self-calibration, we expect to measure Ω_m to ± 0.03 (and Ω_Λ to the same accuracy assuming flatness), and σ_8 to ± 0.05 , also constraining the normalization and slope of the luminosity–temperature relation to ± 6 and ± 13 per cent (at 1σ) respectively in the process. Self-calibration fails to jointly constrain the scatter and redshift evolution of the luminosity–temperature relation significantly. Additional archival and/or follow-up data will improve on this. We do not expect measurement errors or imperfect knowledge of their distribution to degrade constraints significantly. Scaling-relation systematics can easily lead to cosmological constraints 2σ or more away from the fiducial model. Our treatment is the first exact treatment to this level of detail, and introduces a new ‘smoothed ML’ estimate of expected constraints.

Key words: cosmological parameters – cosmology: observations – cosmology: theory – galaxies: clusters: general – methods: statistical – X-rays: galaxies: clusters

* m.sahlen@sussex.ac.uk

† <http://xcs-home.org>

1 INTRODUCTION

The abundance of galaxy clusters as a function of mass and redshift can give a powerful constraint on cosmological models. Specifically, data on the evolution of the number density of galaxy clusters with redshift has been used to obtain direct estimates for both σ_8 , the dispersion of the mass field smoothed on a scale of $8 h^{-1}$ Mpc, and on Ω_m , the present mean mass density of the Universe (Frenk et al. 1990; Oukbir & Blanchard 1992; Viana & Liddle 1996; Oukbir & Blanchard 1997; Henry 1997; Bahcall, Fan & Cen 1997; Eke et al. 1998; Reichart et al. 1999; Donahue & Voit 1999; Viana & Liddle 1999; Blanchard et al. 2000; Henry 2000; Borgani et al. 2001; Refregier, Valtchanov & Pierre 2002; Henry 2004; Gladders et al. 2007; Rozo et al. 2007a). Furthermore, such data could be used to constrain the present energy density of a dark energy component, Ω_w , and its equation of state (Wang & Steinhardt 1998; Haiman, Mohr & Holder 2001; Huterer & Turner 2001; Levine, Schulz & White 2002; Weller, Battye & Kneissl 2002; Battye & Weller 2003; Hu 2003; Majumdar & Mohr 2003, 2004; Wang et al. 2004; Lima & Hu 2005; Mantz et al. 2008), or more simply the present vacuum energy density associated with a cosmological constant, $\Omega_\Lambda \equiv \Lambda/3H_0^2$ (Holder, Haiman & Mohr 2001). Others have suggested using galaxy clusters to constrain particle physics beyond the Standard Model (e.g. Wang et al. 2005; Erlich, Glover & Weiner 2008), or modified-gravity models where it has been shown that e.g. the Dvali–Gabadadze–Porrati (DGP) modified-gravity model should be testable in coming surveys (Tang et al. 2006; Schäfer & Koyama 2008). An alternative method to abundance evolution using X-ray galaxy clusters to constrain cosmology, is based on the gas mass fraction (e.g. Allen, Schmidt & Fabian 2002; Vikhlinin et al. 2003; Ettori, Tozzi & Rosati 2003; Rapetti, Allen & Weller 2005; Vikhlinin et al. 2006; Allen et al. 2008; Rapetti et al. 2008).

Galaxy cluster measurements are complementary to other cosmological constraints derived from the Cosmic Microwave Background (CMB) and distant Type Ia Supernovae observations, and thus help break degeneracies amongst the various cosmological parameters (Bahcall et al. 1999; Haiman et al. 2001; Huterer & Turner 2001; Levine et al. 2002; Battye & Weller 2003; Melchiorri et al. 2003; Wang et al. 2004).

Several surveys have been proposed with the explicit aim of significantly increasing the number of known distant clusters of galaxies. These proposals rely on a variety of detection methods across a wide range of wavelengths: the Sunyaev–Zel’dovich (SZ) effect in the millimeter (see Carlstrom, Holder & Reese 2002 for a review, and Juin et al. 2005 for a list of proposed surveys); galaxy overdensities in the visible/infrared (e.g. Gladders & Yee 2005; Hsieh et al. 2005; Rozo et al. 2007b); bremsstrahlung emission by the intracluster medium (ICM) in the X-rays (e.g. Jahoda & the DUET collaboration 2003; Haiman et al. 2005; Pierre et al. 2008). Galaxy cluster identification using weak lensing techniques is another possibility (e.g. Wittman et al. 2006), but is still in its infancy. Many of these proposals, in particular those regarding the detection of distant clusters through their X-ray emission, imply the building of new observing facilities such as *eROSITA* (Predehl et al. 2006), that will likely take many years to yield results. The cluster X-ray temperature is one of the best proxy observables in lieu of mass; it is a better estimator of the cluster mass than the cluster X-ray luminosity (e.g. Balogh et al. 2006; Zhang et al. 2006) (but more difficult to determine), and galaxy clusters are also most unambiguously identified in X-ray images. This makes X-ray-based galaxy cluster surveys those with

the most accurately determined selection function. For all these reasons, we have undertaken to construct a galaxy cluster catalogue, called *XCS: XMM Cluster Survey*, based on the serendipitous identification of galaxy clusters in public *XMM–Newton* (*XMM*) data (Romer et al. 2001).

The aim of this paper is to forecast the expected galaxy cluster samples from the XCS and, based on those, its ability to constrain cosmology and cluster scaling relations using only self-calibration. Specifically, we consider the expected constraints on Ω_m , σ_8 and the luminosity–temperature relation for a flat Universe. Our results represent the statistical power expected to be present in the full *XMM* archive. This work builds upon previous efforts in several ways, and to a large extent constitutes the first coherent treatment of effects and methods previously only considered separately. Specifically, we combine all the following characteristics:

- (i) we use a Monte Carlo Markov Chain (MCMC) approach and can thus characterize all degeneracies exactly (in contrast to Fisher matrix analyses),
- (ii) we include scatter in scaling relations in the parameter estimation (enabled by MCMC),
- (iii) we include a detailed, simulated selection function (essentially that of the *XMM* archive), not a simple hard flux/photon-count/mass limit,
- (iv) we include realistic photometric redshift errors, including degradation and catastrophic errors,
- (v) we include temperature measurement errors, partly based on detailed simulations of *XMM* observations, and propagate the redshift errors to the temperature, and,
- (vi) we investigate quantitatively the effect on cosmological constraints from systematic errors in cluster scaling relation and measurement error characterization.

Our work builds on the galaxy cluster survey exploitation methods developed and studied primarily in Haiman et al. (2001); Holder et al. (2001); Levine et al. (2002); Hu & Kravtsov (2003); Hu (2003); Battye & Weller (2003); Majumdar & Mohr (2003, 2004); Lima & Hu (2004); Wang et al. (2004); Lima & Hu (2005). Forecasted cosmological constraints from *XMM* data have also been considered for the *XMM–LSS* survey in Refregier et al. (2002), but they did not take into account scaling-relation scatter or measurement errors, and used the Press–Schechter mass function. The most relevant precursors to this paper are Haiman et al. (2001) and Majumdar & Mohr (2004), who consider cosmological constraints expected from the *Dark Universe Exploration Telescope* (*DUET*) (Jahoda & the DUET collaboration 2003) – a 10000 deg² X-ray survey with flux limit $\sim 5 \times 10^{-14}$ erg s⁻¹ cm⁻² in the 0.5–2 keV band. We extend the methodology of both papers through each of the six points above, either by more detailed modeling or by obtaining more robust results through the use of MCMC. Other relevant works are Huterer et al. (2004, 2006) and Lima & Hu (2007), who discuss photometric redshifts. We particularly complement these analyses through our detailed treatment/inclusion of measurement errors and selection effects. The recent work by Rapetti et al. (2008) takes an approach similar to ours in that they employ MCMC, include scaling-relation scatter and consider measurement errors, but focuses on combining future X-ray gas mass fraction measurements with SZ cluster and CMB power spectrum data.

The structure of this paper is as follows. We begin by reviewing the progress to date of the XCS and present the survey selection function (Sect. 2). Next, we present the models and methodology we use to derive constraints on cosmological parameters from the

simulated XCS sample (Sects. 3 & 4). We then go on to the expected cluster distributions and, our estimates for the constraints on σ_8 , Ω_m , and cluster scaling relation parameters that we expect to obtain from the XCS using self-calibration, including the effect of temperature measurement errors and relying on photometric methods to obtain XCS galaxy cluster redshifts (Sect. 5). We discuss and summarize our findings in Sect. 6. Additional material setting out modeling details is provided in the Appendix.

2 THE XMM CLUSTER SURVEY

2.1 Background and current status

XMM-Newton is the most sensitive X-ray spectral imaging telescope deployed to date. It is typically used in pointing mode, whereby it observes a single central target for a long period of time (the typical exposure time being ~ 20 kilo-seconds). The field of view of the *XMM* cameras is roughly half a degree across, so that a considerable area around the central target is observed ‘for free’ during these long pointings. Already many thousands of these pointings are available in the public *XMM* archive. The XCS is exploiting this archive by carrying out a systematic search for serendipitous detections of clusters of galaxies in the outskirts of *XMM* pointings (Romer et al. 2001). Once a cluster candidate has been selected from the archival imaging data, it is then followed up using optical imaging and/or optical spectroscopy, to confirm the identification of the X-ray source and to measure redshifts (see Sect. 3.4). For those XCS clusters that were detected with sufficient counts, an X-ray spectroscopy analysis is carried out, again using the archival data, in order to measure the temperature of the hot intracluster medium (ICM). These temperatures can then be used to study cluster scaling relations and/or to estimate the mass of the cluster (see Sects. 3.2 & 3.3).

The XCS project is ongoing, but already more than 2000 *XMM* pointings have been analysed, yielding a cluster candidate catalogue numbering almost 2000 entries. So far, the XCS covers a combined area of 132 deg^2 suitable for cluster searching and for which optical follow-up has been completed; i.e. this area excludes overlapping and repeat exposures, regions of low Galactic latitude, the Magellanic clouds, and pointings with very extended central targets. Around 75–100 clusters with > 500 photons and $T > 2 \text{ keV}$ are present in this initial area. With many thousand more *XMM* pointings waiting to be analysed by the XCS, and a mission lifetime extending to 2013, a conservative estimate for the final XCS area for cluster searching is 500 deg^2 . We use 500 deg^2 herein for XCS cosmology forecasting (see Table 1), assume a redshift range of $0.1 \leq z \leq 1$, and temperatures of $2 \text{ keV} \leq T \leq 8 \text{ keV}$. We further limit our representative survey to clusters with photon counts > 500 (^{500}XCS hereafter), so that we can be sure to estimate X-ray temperatures with reasonable accuracy (see Sect. 3.5). The lower redshift limit is associated with cluster extents becoming too large, and the cosmic volume also becoming small. The maximum redshift is chosen so that the luminosity–temperature relation can still be reliably modelled/estimated (see Sect. 3.3.3). The temperature range is chosen such that we can expect i) a small contamination from galaxy groups (which typically have temperatures $T < 2 \text{ keV}$), yet include as many of the numerous low-temperature clusters as possible, and ii) that clusters above the high-temperature limit are sufficiently rare that none can be expected. The final cluster catalogue (without the cut-offs defined above for ^{500}XCS) will contain several thousand clusters

Survey	^{500}XCS
Sky coverage	500 deg^2 (serendipitous)
Redshift coverage	$0.1 - 1.0$
X-ray temperature coverage	$2 - 8 \text{ keV}$
Min. photon count	500
X-ray flux limit	By selection function ^a

^a The flux limit is $\sim 3.5 \times 10^{-13} \text{ erg s}^{-1} \text{ cm}^{-2}$ in the $[0.1, 2.4] \text{ keV}$ band, if defined as a probability of detection greater than or equal to 50 per cent. See also Sect. 5.2.1 and Fig. 9.

Table 1. Survey specifications.

out to a redshift of $z \approx 2$. The highest-redshift cluster discovered by the XCS so far is XMMXCS J2215.9-1738 at $z = 1.457$ (Stanford et al. 2006; Hilton et al. 2007).

In addition to producing one of the largest samples of X-ray clusters ever compiled, the XCS will also be a valuable resource for cosmology studies (see Sect. 4). This is because the catalogue will be accompanied by a complete description of the selection function. In this work we make use of an initial XCS selection function that assumes simple models for the distribution of the ICM, and flat cosmologies (see below). Future cosmology analyses will take advantage of more sophisticated selection functions that are based on hydrodynamical simulations of clusters (Kay et al. 2007).

2.2 The XCS selection function

2.2.1 Model

In order to properly model the selection function of a survey like the XCS, it is important to account for all of the observational variations present in real data. We can achieve this by placing a sample of fake surface-brightness profiles into real *XMM* Observation Data Files (ODFs). This ensures that our simulated images recreate real-life issues such as clusters lying on chip gaps and point-source contamination. The fake surface-brightness profiles are created as follows. We use an isothermal β model with $\beta = 2/3$, core radius $r_c = 160 \text{ kpc}$ (close to the mean values of $\beta = 0.64$, $r_c = 163 \text{ kpc}$ obtained from a uniform *ROSAT* analysis of clusters from $0.1 < z < 1.0$; Ota & Mitsuda 2004), and plasma metallicity $Z = 0.3Z_\odot$. For a given cosmology we simulate 700 sets of cluster parameters:

- 10 redshifts (linearly spaced $0.1-1.0$)
- 10 luminosities (log. spaced $0.178-31.623 \times 10^{44} \text{ erg s}^{-1}$)
- 7 temperatures (linearly spaced $2-8 \text{ keV}$)

For selection function determination, we drew on a list of 1764 ODFs that have already been processed by the XCS and have been deemed to be suitable for cluster searching (see above). Before each selection function run, a smaller list of 100 ODFs is selected at random from the full set of 1764. These 100 ODFs are then copied from the main XCS archive to local processing nodes for temporary storage, to speed up the analysis. Tests have shown that with 100 ODFs it is still possible to reproduce the variance in exposure time, target type, point source density, etc., inherent to the XCS. In the following we define a ‘selection function run’ as the analysis over the 700 sets of cluster parameters and 100 ODFs – a total of 70000 combinations.

For each of the 700 different combinations of cluster parameters, the process proceeds as follows. First, to account for the fact

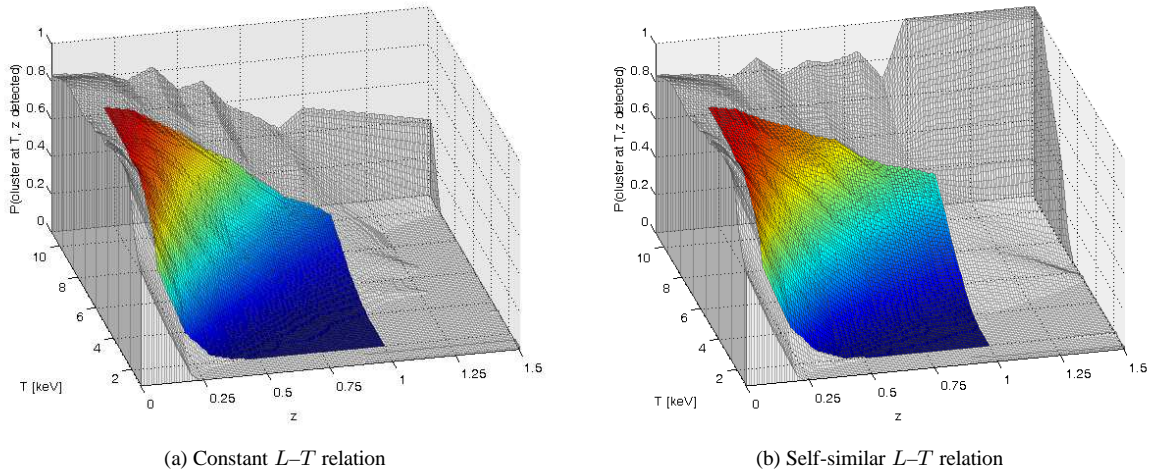


Figure 1. Selection function for our fiducial cosmology and different L - T evolution. Values in the shaded region are extrapolated from those in the coloured region ($0.1 \leq z \leq 1.0$, $2 \text{ keV} \leq T \leq 8 \text{ keV}$), for which the selection function has been calculated explicitly.

that the XCS searches the entire field of view for serendipitous cluster detections, the centre of the fake surface-brightness profile is randomly positioned into a blank *XMM*-style ODF, with a uniform probability across the field of view. The profile is then convolved with the appropriate PSF model. For this purpose we use the two-dimensional medium-accuracy model¹. At this stage, an ODF is chosen at random from the list of 100 stored locally, into which the fake source will later be added. The profile is then assigned an absorbed count rate using a series of arrays calculated using XSPEC (Arnaud 1996). The arrays tabulate conversions from unabsorbed bolometric luminosity to absorbed count-rate as a function of temperature, redshift, hydrogen column density, and *XMM* camera/filter combination. The fake count-rate image is then multiplied by the exposure map of the chosen ODF to account for vignetting, masking and chip gaps. Finally, the fake cluster image is added to the original ODF at the chosen position, and the ODF is run through our source detection/classification pipeline to determine if the fake cluster passes our automated cluster-candidate selection process. For more details on the detection/classification pipeline, refer to Davidson et al. (in preparation). The process is repeated a total of one hundred times, so that we can build up an average XCS detectability for that parameter combination. Once the full set of 700 combinations has been tested 100 times each, the run is complete. We then change the cosmology inputs and start the entire sequence again. The process is very CPU intensive; each selection function run (of 700×100 combinations) takes several weeks to run on a single node. For the forecasting work presented herein, we carried out seven selection function runs over the flat Λ CDM cosmologies with $\Omega_m = 0.22, 0.26, 0.28, 0.30, 0.32, 0.34$ and 0.38 . We limit ourselves to flat cosmologies as we use a flatness prior in the forecasting of cosmological constraints.

The resulting selection function is shown in Fig. 1 for the two luminosity-temperature relations (see Sect. 3.3.1) we consider. Note that the selection function in regions where we have not calculated it explicitly is extrapolated from the region where we have done so. Hence, its features in those extrapolated regions should only be considered a rough indication of its behaviour, particularly

in the high-redshift, high-temperature region. This region is only relevant for including measurement errors, and since such high-temperature clusters are exceedingly rare, the uncertainty in this part of the selection function has no significant impact on our results².

2.2.2 Uncertainty

The shape of the selection function is dependent on the cluster model employed, as described above. It is well known that clusters of galaxies have a range of morphologies, with core radii varying from many tens of kpc to a few hundred kpc and β values varying generally between 0.45 and 0.85 (e.g. Reiprich & Böhringer 2002; Ota & Mitsuda 2004; Maughan et al. 2008).

To include the variation of cluster-model parameters in our analysis in a realistic manner, one would require i) a model for the distribution of such parameters among the cluster population (including correlations among parameters), and ii) a characterization of the selection function dependence on such parameters. Lacking either or both of these will produce some level of uncertainty in cluster number predictions and cosmological parameter constraints. However, assessing the level of such uncertainty of course requires a fiducial model (realizing i) and ii)) to compare with. As we do not currently have a realistic model for the model-parameter distribution among the cluster population, it is somewhat premature to carry out such an analysis. In actual data analysis, we intend to model this in detail. What we can currently do is to compare our standard selection function to one assuming that all clusters have the most extreme values of cluster-model parameters, leading to a gross overestimation of the overall uncertainty in cluster number predictions. We have carried this calculation out for clusters with temperatures typical for the underlying distribution at different redshifts, and describe it below. We again stress that its usefulness for estimating the actual uncertainty in the selection function is limited, as it does not take into account the actual distribution of clusters and their model parameters. Ultimately, we expect that

¹ http://xmm.vilspa.esa.es/external/xmm_sw_cal/calib/

² We have subsequently verified the validity of the extrapolation to this level of accuracy with new calculations.

the cosmological constraints we obtain would change little, even if a more realistic model/selection function was used. This is because the changes in the selection function would have a similar impact for the fiducial cosmological model, and for models in its neighbourhood.

We have tested the sensitivity of the selection function for clusters with > 500 photons to variations in the cluster core radius r_c , between the values of 60 kpc and 260 kpc (recall the fiducial value used in this work is 160 kpc, see Sect. 2.2.1). For this we use mock clusters with typical temperatures of $T = 3$ keV (and hence luminosities) for a given redshift (as predicted by our models, see Sects. 3 & 4). In the following, we refer to the relative difference in the selection function detectability, as this is most relevant to the relative difference in numbers of clusters. Our results show that, for most of the redshift range tested ($0.1 \leq z \leq 1$), clusters with a core radius of ~ 140 kpc are easier to detect (as extended *XMM* sources), than those with smaller or larger core radii. However, the dependence is shallow; the relative uncertainty in the detectability is less than 10 per cent up to a redshift of $z \sim 0.4$, across the entire r_c range. At higher redshifts, the relative uncertainty approaches 30–40 per cent. However, this subset of clusters constitutes only ~ 30 per cent of the total population. For higher-temperature clusters, the relative uncertainty drops back to around 10 per cent at $0.1 \leq z \leq 1$ for $4 \text{ keV} \leq T \leq 5 \text{ keV}$.

In summary, our model for the cluster population is a simplification based on mean observational values of cluster-model parameters, and as a result will have somewhat differing detection properties compared to a real sample. To characterize such uncertainty requires modelling of the cluster-model parameter distribution, and the selection function dependence on those parameters. However, once such information becomes available, it will be included in the analysis and hence remove/reduce such uncertainty. As we do not currently have a realistic model of the cluster parameter distribution, we have determined the impact of assuming extreme structural cluster parameters, and found that at most the typical selection function uncertainty is of the order of 10 per cent. These results agree with those of Burenin et al. (2007) for the 400d survey, which show that reasonable variations in cluster size, morphology and scaling relations induce an uncertainty in the detectability for a given flux of typically less than 5 per cent.

3 FROM X-RAY OBSERVABLES TO MASS

3.1 Modeling summary

Making predictions for X-ray cluster observations requires the modeling of scaling relations to relate temperature to mass, and temperature to luminosity. In addition, the observables will have uncertainties associated with them, which need to be taken into account. The following subsections detail our modeling assumptions, but we summarize them here for reference and orientation.

We first assume that we know *a priori* exactly how the cluster X-ray temperature relates to luminosity at the present time, and how this relation evolves with redshift. We then study how the constraints on cosmological parameters degrade if such an assumption is dropped. We consider four extra free parameters: two parameters to characterize the present-day, power-law, relation between cluster X-ray temperature and luminosity, another to describe its redshift evolution as a power of $(1+z)$, and lastly one for the logarithmic dispersion in the (assumed) Gaussian distribution of the intrinsic (redshift-independent) scatter in the relation between cluster X-ray temperature and luminosity.

In addition, we evaluate the full impact on the XCS's ability to impose constraints on cosmological parameters that arises from assuming a dispersion in the Gaussian photometric redshift distribution of either 5 or 10 per cent about the true redshift, both with and without the presence of unaccounted-for catastrophic errors in the photometric redshift estimation procedure. Further, we will also determine the impact of a systematic mis-estimation of the assumed true dispersion in the photometric redshifts about the true redshift. Our aim is to test the impact of realistic assumptions regarding the distribution of photometric redshifts around the true redshift, and then determine by how much such impact increases by considering a worst-case scenario.

Similarly, we consider the impact of realistic X-ray temperature errors obtained from simulations based on the relevant *XMM* fields, as well as significantly larger errors corresponding to a worst-case scenario. Lastly, we consider the impact of incorrect assumptions about the cluster scaling relations on cosmological constraints.

Summary tables with our main cluster scaling relation and measurement error assumptions are given in Sect. 5. Detailed information on the mathematical treatment is given in the Appendix.

3.2 The X-ray temperature to mass relation

We need to assume a relation between cluster X-ray temperature and mass to be able to predict cluster distributions. The reason is that presently the effect of cosmological parameters on the galaxy cluster population can only be accurately predicted as a function of cluster mass (e.g. Reiprich & Böhringer 2002). The X-ray temperature is one of the best proxy observables, as explained in the Introduction.

3.2.1 Evolution

We assume the self-similar prediction (e.g. Kaiser 1986; Bryan & Norman 1998; Voit 2005a),

$$T \propto M_v^{2/3} [\Delta_v(z) E^2(z)]^{1/3}, \quad (1)$$

for the redshift dependence of the relation between cluster X-ray temperature and virial mass to hold for any combination of cosmological parameters, given that it is consistent with the most recent analyses of observational data (Ettori et al. 2004a,b; Arnaud, Pointecouteau & Pratt 2005; Kotov & Vikhlinin 2005, 2006; Vikhlinin et al. 2006; Zhang et al. 2006). Here M_v is the cluster virial mass, while $\Delta_v(z)$ is the mean overdensity within the cluster virial radius with respect to the critical density. If the only relevant energy densities in the Universe are those associated with non-relativistic matter and a cosmological constant, then

$$E^2(z) = \Omega_m(1+z)^3 + \Omega_k(1+z)^2 + \Omega_\Lambda, \quad (2)$$

with $\Omega_k = 1 - \Omega_m - \Omega_\Lambda$. (Note that we will restrict ourselves to a flat Universe, $\Omega_k = 0$, in our analysis – see Sect. 4.2). Deviations from a self-similar mass–temperature relation will be considered in Sect. 5.5, as explained in the following Section.

3.2.2 Normalization

The constant of proportionality is set by demanding that for our fiducial cosmological model (with $\sigma_8 = 0.8$, see Sect. 4.2)

$$M_{500} = 3 \times 10^{14} h^{-1} M_\odot \quad (3)$$

at $z = 0.05$ for an X-ray temperature of 5 keV, where M_{500} is the mass within a sphere centered on the cluster within which its mean density falls to 500 times the critical density at the cluster redshift. In this way, our fiducial cosmological model reproduces the local abundance of galaxy clusters as given by the HIFLUGCS catalogue (Reiprich & Böhringer 2002; Pierpaoli, Scott & White 2001; Viana et al. 2003). Note that such a normalization of the cluster X-ray temperature to mass relation happens to be very close to that directly derived from X-ray data by Arnaud et al. (2005) and Vikhlinin et al. (2006).

The conversion between M_{500} and the halo mass, $M_{180\Omega_m(z)}$, will be carried out by using the formulae derived by Hu & Kravtsov (2003) under the assumption that the halo density profile is of the NFW type (Navarro, Frenk & White 1995, 1996, 1997), and we will take the concentration parameter to be 5. This has been shown to provide a good description of the typical density profile in galaxy clusters (see Arnaud 2005 or Voit 2005b and references therein; Vikhlinin et al. 2006).

The normalization of the M – T relation is subject to a number of uncertainties, the most important of which are the possible violation of hydrostatic equilibrium (Rasia, Tormen & Moscardini 2004; Nagai, Kravtsov & Vikhlinin 2007) and the possible difference between the spectroscopic X-ray temperature and the temperature of the electron gas (Mazzotta et al. 2004; Rasia et al. 2005; Vikhlinin 2006). The precise level of these effects remains to be firmly established, but could be of the order 50% in the normalization mass (e.g. Vikhlinin 2006; Nagai et al. 2007). The scatter, as well as slope, could also be under-estimated due to these effects (Vikhlinin 2006; Nagai et al. 2007). We make some estimates of all these systematic effects on cosmological constraints in Sect. 5.5.

3.2.3 Scatter

We assume that the intrinsic scatter in the relation between cluster X-ray temperature and mass has a Gaussian distribution (truncated at 3σ and re-normalized) with a redshift-independent dispersion of 0.10 about the logarithm of the temperature. This is motivated by both cluster X-ray data analysis (e.g. Arnaud et al. 2005; Vikhlinin et al. 2006; Zhang et al. 2006) and results from N -body hydrodynamic simulations (e.g. Viana et al. 2003; Borgani et al. 2004; Balogh et al. 2006; Kravtsov, Vikhlinin & Nagai 2006). As explained in the preceding Section, we consider systematic deviations in the scatter in Sect. 5.5.

3.3 The X-ray luminosity to temperature relation

In order to understand how the XCS selection function depends on cluster mass, we need to know how cluster X-ray luminosity and temperature relate to cluster mass (see Sect. 2.2). In practice, we will use the relation between luminosity and temperature instead of that between luminosity and mass, in effect relating these two quantities via the temperature. This makes sense because the estimation of cluster mass from X-ray data is always based on the X-ray temperature, via the assumption of hydrostatic equilibrium, and not on the luminosity. Thus, while we always need, at least implicitly, to know how the cluster luminosity relates to temperature to derive the relation between the luminosity and mass from X-ray data, the reverse is not true.

As for the mass–temperature relation, assuming self-similarity

leads to a specific prediction (Kaiser 1986),

$$L(z, T) = L(0.05, T) \left[\frac{\Delta_v(z) E^2(z)}{\Delta_v(0.05) E^2(0.05)} \right]^{1/2}, \quad (4)$$

under which clusters with the same X-ray temperature are predicted to be more X-ray luminous if they have a higher redshift. We have chosen here to normalize the relation with respect to the local ($z = 0.05$) relation. Based on this expression, we write the L – T relation in the general form

$$\log_{10} \left(\frac{L_X}{10^{44} h^{-2} \text{ erg s}^{-1}} \right) = \alpha + \beta \log_{10} \left(\frac{kT}{1 \text{ keV}} \right) + \gamma_s \log_{10} [\Delta_v(z) E^2(z)] + \gamma_z \log_{10} (1+z) + N(0, \sigma_{\log L_X}). \quad (5)$$

and discuss below the assumptions made for the different parameters.

3.3.1 Evolution (γ_s, γ_z)

We consider two possible fiducial scenarios, which bracket most observational results and theoretical expectations: either

- no evolution ($\gamma_s = \gamma_z = 0$) or
- self-similar evolution ($\gamma_s = 1/2, \gamma_z = 0$)

for the fiducial combination of cosmological parameters. The parameters γ_s and γ_z are defined above in equation (5). Presently, there is some uncertainty surrounding the redshift evolution of the relation between cluster X-ray luminosity and temperature. Essentially, what we know is how that relation behaves for redshifts below 0.3 (e.g. Ikebe et al. 2002; Novicki, Sornig & Henry 2002; Ota et al. 2006; Zhang et al. 2006). For higher redshifts, the data is still sparse, and the evidence contradictory, from claims that the relation between cluster X-ray luminosity and temperature barely evolves at all with redshift (Holden et al. 2002; Ettori et al. 2004a,b; Ota et al. 2006; Branchesi et al. 2007), to claims that its evolution is close to the self-similar prediction (Novicki et al. 2002; Vikhlinin et al. 2002; Lumb et al. 2004; Kotov & Vikhlinin 2005; Maughan et al. 2006; Zhang et al. 2006; Hicks et al. 2008). Some authors argue that self-similarity remains viable at all redshifts, and that at least some of the observed discrepancies could be due to selection effects, as the Malmquist bias from scaling-relation scatter (also discussed below) could distort the deduced evolution if the sample selection is not sufficiently understood (e.g. Branchesi et al. 2007; Maughan 2007; Pacaud et al. 2007; Nord et al. 2008). On the other hand, Hilton et al. (2007) argue for deviation from the self-similar prediction based on a set of high-redshift clusters combined with the recently discovered XCS cluster XMMXCS J2215.9-1738 at $z = 1.457$.

When the XCS catalogue becomes available, the relation between cluster X-ray luminosity and temperature, as a function of redshift, will be estimated jointly with the cosmological parameters, but for now we will have to rely on the limited information available.

3.3.2 Normalization & slope (α, β)

We assume the local ($z = 0.05$) relation between the cluster X-ray luminosity in the *ROSAT* [0.1, 2.4] keV band and temperature to be

$$\log_{10} \left(\frac{L_X}{h^{-2} \text{ erg s}^{-1}} \right) = 42.1 + 2.5 \log_{10} \left(\frac{kT}{1 \text{ keV}} \right), \quad (6)$$

as was derived in Viana et al. (2003) for a combination of cosmological parameters similar to those assumed for our fiducial cosmological model. The X-ray data used in Viana et al. (2003) was that of galaxy clusters present in the HIFLUGCS catalogue (Reiprich & Böhringer 2002), and therefore the conversion between L_X and X-ray bolometric luminosity is performed through a fit (derived by us) based on the values both quantities take for the galaxy clusters in HIFLUGCS,

$$L_{\text{bol}} = \frac{L_X}{0.25 + 0.7 \exp(-0.23kT/1 \text{ keV})}. \quad (7)$$

As in Ikebe et al. (2002), the relation between the cluster X-ray luminosity and temperature derived in Viana et al. (2003) takes into account the fact that any flux-limited sample of galaxy clusters will be composed of objects which are on average more X-ray luminous than the mean luminosity of all existing galaxy clusters with the same redshift and X-ray temperature. This Malmquist type of bias increases with decreasing temperature, and thus ignoring it leads not only to an overestimation of the normalization of the relation between luminosity and temperature, but also to an underestimation of its slope.

3.3.3 Scatter ($\sigma_{\log L_X}$)

We assume that the intrinsic scatter in the relation between cluster X-ray luminosity (in the 0.1 to 2.4 keV band) and temperature has a redshift-independent Gaussian distribution (truncated at 3σ and re-normalized) about the logarithm of the X-ray luminosity, with 1σ dispersion $\sigma_{\log L_X} = 0.30$ (Ikebe et al. 2002; Viana et al. 2003). This is also close to what was found by Kay et al. (2007) in the CLEF simulation. Although Kay et al. also observe an evolution of the scatter with redshift, there is no strong observational evidence for or against such an evolution at present, and therefore we do not include it in our analysis.

The existence of intrinsic scatter in the relation between cluster luminosity and mass will effectively increase the observed number of galaxy clusters above any X-ray luminosity (or flux) threshold, relative to the case without scatter. This results from the steepness of the cluster mass function, due to which significantly more clusters have their X-ray luminosity scattered up than down across any given luminosity threshold. Therefore, intrinsic scatter between X-ray luminosity and mass can have a considerable impact on the predicted number of XCS clusters and on the estimation of the constraints the XCS will impose on cosmological parameters. This scatter can be considered as the combination of the scatter in the luminosity to temperature and temperature to mass relations, with clear observational evidence that the former dominates over the latter (Stanek et al. 2006; Zhang et al. 2006).

As higher redshifts are considered, it is expected that an increasing number of galaxy clusters will have undergone recent major mergers, not only leading to increased scatter in the cluster scaling relations but also making its distribution highly non-Gaussian, with long tails developing towards both high X-ray luminosity and, to a lesser degree, temperature, at fixed mass (Randall, Sarazin & Ricker 2002). This has the potential to substantially affect the estimation of the constraints the XCS will be able to impose on cosmological parameters. There is a lack of high-redshift observational data in this regard and we are also not confident that we will detect, for the purposes of understanding this behaviour, many useful clusters at $z > 1$. We therefore chose to consider in the estimation procedure only those clusters in the mock XCS catalogues which have a redshift $z \leq 1$.

3.4 Photometric redshifts

3.4.1 The role of photometric redshifts

Redshifts are required for XCS clusters, both to place them correctly in the evolutionary sequence and to allow the measurement of X-ray temperatures from *XMM* spectra. With regard to the latter point, pure thermal bremsstrahlung spectra are essentially featureless (barring a high-energy cut-off), making them degenerate in temperature and redshift. Therefore, in the absence of independent redshift information, all one can measure from a typical XCS cluster spectrum would be a so-called apparent X-ray temperature, i.e. one scaled by $(1+z)$, see Appendix A1.2. As shown by Liddle et al. (2001), these apparent temperatures are not sufficient to allow one to measure cosmological parameters from cluster catalogues. As a result, optically-determined redshifts will be required for almost all clusters in the XCS catalogue (the exception being a tiny number that are detected with sufficient signal to noise to allow X-ray emission features, such as the Iron K complex at ~ 7 keV, to be resolved over the thermal continuum).

As is now typical for cluster surveys (e.g. Gladders & Yee 2005), the XCS is relying heavily on the photometric redshift technique for its optical follow-up. This is because photometric redshifts are much more efficient, in terms of telescope time requirements, than spectroscopic redshifts. However, they have the disadvantage, over spectroscopic redshifts, that the redshift errors are larger and sometimes poorly understood. The XCS is using both public-domain photometry (e.g. from SDSS and 2MASS) and proprietary data from the NOAO-XCS Survey (NXS, Miller et al. 2006) to both optically confirm (as clusters) XCS candidates and to measure photometric redshifts. To date, more than 400 XCS candidates have been optically confirmed in this way.

Errors on photometric redshifts must be accounted for when determining cosmological parameters from cluster surveys, and so we have included prescriptions for such errors in the forecasting work presented herein. Our prescriptions include both purely statistical errors and so-called catastrophic systematic errors. As shown by previous work (Huterer et al. 2004, 2006; Lima & Hu 2007), purely statistical errors have a negligible impact on cosmological parameter constraints. By contrast, if catastrophic errors are not accounted for properly in the fitting, they could have a significant impact on cosmological parameter constraints. We note that previous work has concentrated only on the impact of redshift errors on the evolutionary sequence, whereas we have also included the impact of photometric errors on X-ray temperature determinations.

3.4.2 Distribution

Following Huterer et al. (2004) we assume that the statistical error in the photometric redshifts of individual galaxy clusters has a Gaussian distribution about the true redshift, z_t . In an attempt to reproduce the expected degradation with redshift of the absolute accuracy of cluster photometric redshift estimation methods, and in contrast to Huterer et al. (2004) (but in the same way as Lima & Hu 2007), we will assume the dispersion to be proportional to $(1+z_t)$, normalized at $z_t = 0$ to either $\sigma_0 = 0.05$ or $\sigma_0 = 0.10$ (Gladders & Yee 2000; Gladders 2004; Gladders & Yee 2005; Gladders et al. 2007). Unaccounted-for systematic errors in the photometric redshift estimation procedure are much harder to model, because they can take a variety of guises. We will consider here one such type of error: catastrophic errors in the photometric redshift estimation procedure. The existence of unaccounted-for

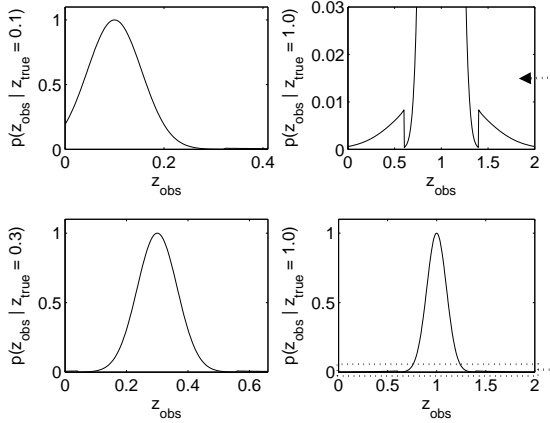


Figure 2. Realistic redshift error distributions at various redshifts. The upper right panel shows a magnification of the bottom-right distribution, highlighting the catastrophic-error part of the distribution.

catastrophic errors will be modelled by assigning a random photometric redshift error to either a fraction $f_{\text{cat}} = 0.05$ or $f_{\text{cat}} = 0.10$ of the galaxy clusters, drawn from a Gaussian distribution that has four times the dispersion of the standard distribution, with the requirement that the photometric redshift error has to be at least 1σ away from the true redshift. The functional form of the redshift error distribution is given in Appendix A1.

We label the case $\{\sigma_0 = 0.05, f_{\text{cat}} = 0.05\}$ ‘realistic’ and the case $\{\sigma_0 = 0.10, f_{\text{cat}} = 0.10\}$ ‘worst-case’ redshift errors. Examples of realistic redshift error distributions are shown in Fig. 2.

3.5 X-ray temperature

3.5.1 Estimating the measurement errors

Initial estimates (Liddle et al. 2001) showed that X-ray temperatures measured for XCS clusters are expected to have an associated measurement uncertainty of less than 20 per cent at 1σ . However, these estimates were based on a photon count of 1000 and assume a single hydrogen column density over the *XMM* fields, and are therefore not directly applicable to our 500 XCS sample. Hence, in order to estimate the temperature errors that will be present in the XCS statistical sample more accurately, we have conducted Monte Carlo simulations using the XSPEC spectral fitting package (Arnaud 1996). We created 1000 sets of fake spectra for the *XMM-Newton* EPIC PN and MOS instruments, from a MEKAL plasma model (Mewe, Lemen & van den Oord 1986) multiplied by a WABS photo-electric absorption model (Morrison & McCammon 1983). Responses for a mean off-axis angle were used and a mean background was added. The model was then fitted to each of the spectra to derive a temperature. A plasma metallicity of $0.3Z_{\odot}$ was used throughout, in accordance with the assumptions in our selection function calculations (see Sect. 2.2), and we assume a photon count of 500. This procedure was repeated for a range of input temperatures, redshifts and absorption columns. We then marginalize over the hydrogen absorption columns using the expected hydrogen column distribution for our *XMM* fields.

The mean fractional temperature errors from our simulations are shown in Fig. 3. The largest influence on the temperature errors comes from the input temperature itself. Since metal lines in the spectrum provide much better constraints on the temperature than the shape of the bremsstrahlung continuum, and the fraction of line

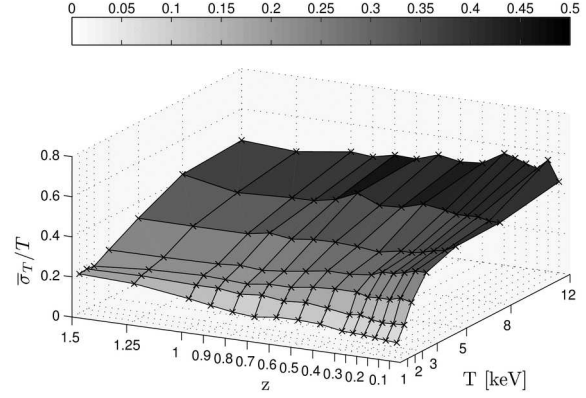


Figure 3. Mean fractional temperature errors from the simulations performed, for 500 photons, and as marginalized over expected absorption columns for the XCS.

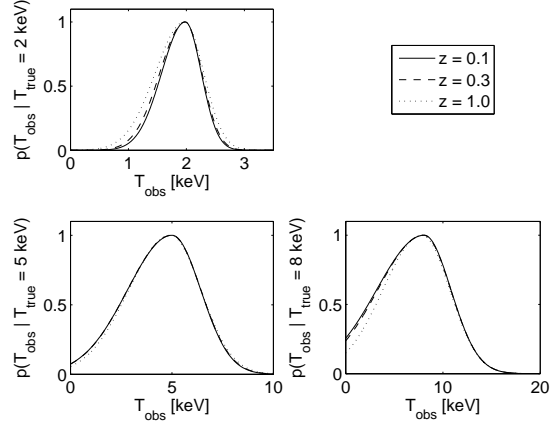


Figure 4. Realistic temperature error distributions at various redshifts and temperatures, based on our *XMM-Newton* simulations, for a photon count of 500.

emission in the spectrum declines with increasing temperature, the errors are larger for hotter clusters. The effect of redshift on the errors is much smaller and itself temperature-dependent. For low-temperature systems at high redshifts, part of the X-ray spectrum is shifted out of the bottom of the *XMM* passband, increasing the errors. For high-temperature systems, the effect of increasing redshift is to shift the source spectrum to lower energies for which the *XMM* effective area is larger, thus decreasing the errors.

3.5.2 Distribution

The distribution of temperatures obtained in our simulations was fitted by an asymmetric Gaussian function to parametrize the temperature error distribution, with the fractional error given by a two-dimensional quadratic expression in temperature and redshift. We marginalize over the distribution of absorption columns found in XCS fields to obtain mean parameters for our asymmetric Gaussian error distribution. The exact functional form of the fitted error distribution is given in equation (A8) in Appendix A1.

We will label the case with σ_T according to our simulation results as ‘realistic’ and the case with three times this dispersion as ‘worst-case’ temperature errors. Examples of realistic temper-

ature error distributions are shown in Fig. 4. Note that, as we are assuming that all detected clusters have a photon count of exactly 500, our error distributions represent a worst-case scenario in this regard.

4 FROM MASS TO COSMOLOGY AND CONSTRAINTS

4.1 The mass function

Having connected our direct X-ray observables to cluster mass using the methodology in the preceding Section, we can then combine these relations with the mass function (below) to find the cluster distribution as a function of temperature and redshift. The differential number density of haloes in a mass interval dM about M at redshift z can be written as

$$n(M, z) dM = -F(\sigma) \frac{\rho_m(z)}{M\sigma(M, z)} \frac{d\sigma(M, z)}{dM} dM, \quad (8)$$

where $\sigma(M, z)$ is the dispersion of the density field at some co-moving scale $R = (3M/4\pi\rho_m)^{1/3}$ and redshift z , and $\rho_m(z) = \rho_m(z=0)(1+z)^3$ the matter density.

4.1.1 Parametrization

It has been shown by Jenkins et al. (2001) that a good fit (accurate to better than 20 per cent) to the mass functions recovered from various large N -body simulations, in the regime $-1.2 \leq \ln \sigma^{-1} \leq 1.05$, is given by

$$F_J(\sigma) = 0.315 \exp[-|\ln \sigma^{-1} + 0.61|^{3.8}], \quad (9)$$

where the halo mass is defined at a mean overdensity of 180 with respect to the background matter density, independently of the cosmological parameters assumed, or equivalently to a mean overdensity of $180\Omega_m(z)$ with respect to the critical density. This result has been confirmed by Evrard et al. (2002); Hu & Kravtsov (2003); Klypin et al. (2003); Linder & Jenkins (2003); Reed et al. (2003); Łokas, Bode & Hoffman (2004); Warren et al. (2006); Reed et al. (2007), and we will therefore use this fit to estimate the expected comoving number density of haloes for any given combination of cosmological parameters. This also makes the like-for-like comparison with other cluster constraints straightforward, as most rely on the Jenkins mass function. The dispersion σ is calculated using a fit in analogue to Viana & Liddle (1999), which is accurate to within two percent for the range of halo masses relevant for this work, compared to the exact expression employing the BBKS transfer function (Bardeen et al. 1986). (In a real data analysis, this prescription would not be sufficiently accurate, however for forecasting purposes it is acceptable.)

4.2 Cosmology

We have already seen that cosmology enters into the prediction of cluster numbers as a function of temperature and redshift through the selection function, the cluster scaling relations, and the mass dispersion. Additionally, the cosmic volume dV/dz will also enter as we need to multiply the differential distribution by this quantity (discussed in the following Section).

Parameter	Value	Prior
Ω_m	0.3	$[0.1, 1]$
Ω_Λ	0.7	$1 - \Omega_m$
σ_8	0.8	$[0.3, 1.3]$
Ω_b	0.044	0.044
h	0.75	0.75
n_s	1	1

Table 2. Cosmology assumptions used. Fiducial values are given first, followed by priors assumed in parameter estimation.

4.2.1 Parameters

We work within the Cold Dark Matter (CDM) paradigm, with a spectrum of primordial adiabatic Gaussian density perturbations. We assume that $\Omega_m = 0.3$, $\Omega_\Lambda = 0.7$, $\sigma_8 = 0.8$, $\Omega_b = 0.044$ and $h = 0.75$. As we do not expect the XCS to have particularly competitive constraining power on Ω_k , we restrict our analysis to the case of a flat universe, $\Omega_k = 0$, in accordance with observations of e.g. the cosmic microwave background (Spergel et al. 2007). We take the present-day shape of the matter power spectrum to be well approximated by a CDM model with scale-invariant primordial density perturbations whose transfer function shape parameter is $\Gamma \approx \Omega_m h \times \exp[-\Omega_b(1 + \sqrt{2}h/\Omega_m)] = 0.18$. This is the mean value obtained from different analyses of SDSS data (Szalay et al. 2003; Pope et al. 2004; Tegmark et al. 2004b; Eisenstein et al. 2005; Blake et al. 2007; Padmanabhan et al. 2007) and also perfectly compatible with the 3-year WMAP data (Spergel et al. 2007). We have checked that assuming Γ is either 0.16 or 0.20 does not change our results. (In a real data analysis, using the shape parameter is too simplistic, but for forecasting purposes it is sufficient.) A summary of our cosmological parameter assumptions is given in Table 2.

4.3 Combining observables and cosmology

As we have seen, our cluster distribution calculations involve many different steps and components. Importantly, they rely on both simulation and observational data, as well as direct theoretical input. A schematic overview of the relevant inputs, processes and outputs is shown in a flowchart form in Fig. 5. Collecting all components, the number of clusters in $dTdz$ around (T, z) is given by

$$n(M(T, z), z) \frac{dM}{dT} f_{\text{sky}}(L(T, z), T, z) \frac{dV}{dz} dT dz \quad (10)$$

where f_{sky} combines survey area and selection function. This expression ignores scatter in the scaling relations and measurement errors. A complete treatment is given in Appendix A1. The remaining component for arriving at parameter constraints is the likelihood, which is described next.

4.4 Likelihood

Turning our attention to using the cluster distribution prediction for cosmological constraints and forecasting, we need an expression for the likelihood of an observed catalogue of galaxy clusters. The likelihood \mathcal{L} for a given observed catalogue is simply the product of the Poisson probabilities of observing N_i XCS clusters in the bin with widths $\Delta T, \Delta z$ centered at each of the (T_i, z_i) positions,

$$\mathcal{L} = \prod_i \left[\frac{\lambda_i^{N_i}}{N_i!} e^{-\lambda_i} \right] \quad (11)$$

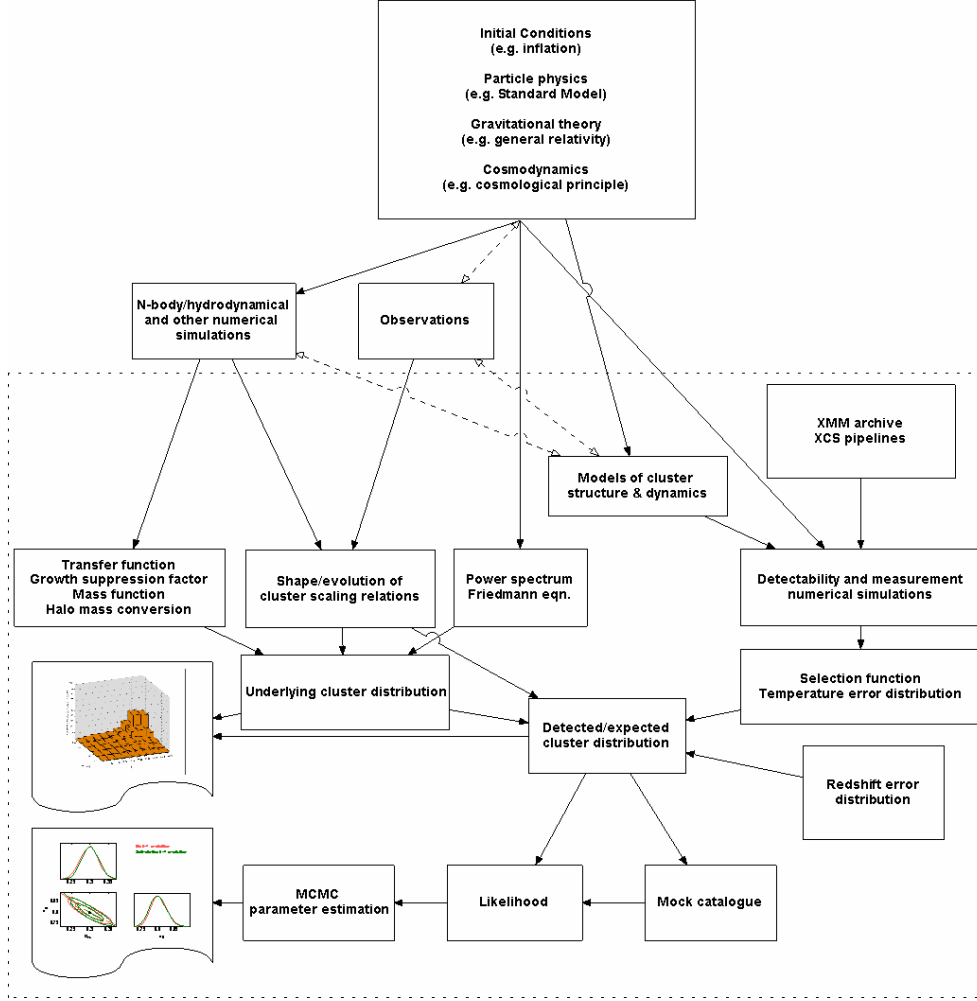


Figure 5. Flowchart for cluster predictions and forecast parameter estimation. The dash-enclosed area indicates the processes that enter in our calculations. Bi-directional dashed arrows are used to indicate the main circular relations, where information from one part is used to inform another, which then informs the first, and so on.

where

$$\lambda_i = N(T_i - \Delta T/2, T_i + \Delta T/2, z_i - \Delta z/2, z_i + \Delta z/2) \quad (12)$$

is the expected number of XCS clusters in bin i , taking into account sky coverage, survey selection function, and any uncertainties in scaling relations or measurements (see equations in Appendix A1). We do not take into account the fact that the positions of galaxy clusters are spatially correlated, because the mean distance between XCS clusters is typically much larger than the observationally determined correlation length in the range $10 - 20 h^{-1}$ Mpc (see e.g. Nichol et al. 1992; Romer et al. 1994; Collins et al. 2000; Gonzalez, Zaritsky & Wechsler 2002; Brodwin et al. 2007), as a result of the *XMM* pointings being scattered all over the sky. Even if the XCS area was contiguous, given the very large depth of the XCS, the impact of cluster spatial correlations on the estimation of cosmological parameters with the XCS galaxy cluster abundance data would be small (White 2002; Hu & Kravtsov 2003; Holder 2006; Hu & Cohn 2006).

As we are seeking to obtain expected/typical constraints, in a sense a Maximum Likelihood (ML) point estimate, we use $N_i = \lambda_i^*$, where the asterisk denotes fiducial-model values. Using this ‘average-catalogue’ construction, we obtain an excellent estimate

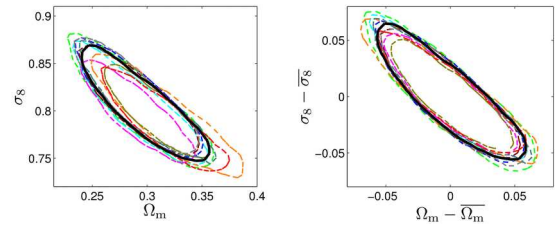


Figure 6. Parameter constraints (95 per cent confidence level) for a set of 10 random realizations of the catalogue Poisson distribution (dashed coloured lines) compared to the average-catalogue parameter constraint (solid black line). In the right-hand panel, each contour has been re-centred around its distribution mean. A constant L – T relation and no L – T or M – T scatter was assumed.

of the size and shape of the expected likelihood contours, but avoid the offset in the best fit away from the fiducial parameter values that is associated with, e.g., the most likely catalogue. Any random realization of a Poisson sample will exhibit such an offset. Examples can be seen in the right-hand panel of Fig. 6, where the results for the average-catalogue method is compared to those for random catalogue realizations. We wish to avoid offsets of this type as we

Parameter	Description	No $L-T$ / $M-T$ scatter Constant $L-T$	No $L-T$ / $M-T$ scatter Self-similar $L-T$	$L-T$ / $M-T$ scatter Constant $L-T$	$L-T$ / $M-T$ scatter Self-similar $L-T$
Colouring		Pink	Green	Orange	Blue
$L-T$:					
α	Normalization	-1.90 [-1.90]	-1.92 [-1.92]	-1.90 flat, unrestricted	-1.92 flat, unrestricted
β	Slope	2.5 [2.5]	2.5 [2.5]	2.5 flat, unrestricted	2.5 flat, unrestricted
γ_s	Self-similarity exp.	0 [0]	$1/2$ [$1/2$]	0 [0]	$1/2$ [$1/2$]
γ_z	Redshift exp.	0 [0]	0 [0]	0 [$-1, 1.5$]	0 [$-1, 1.5$]
$\sigma_{\log L_X}$	Scatter	0 [0]	0 [0]	0.3 [$0.2, 0.4$]	0.3 [$0.2, 0.4$]
m_L	Max. scatter in units of $\sigma_{\log L_X}$	–	–	3 [3]	3 [3]
$M-T$:					
evolution		self-similar, normalized to HIFLUGCS			
$\sigma_{\log T}$	Scatter	0 [0]	0 [0]	0.1 [0.1]	0.1 [0.1]
m_T	Max. scatter in units of $\sigma_{\log T}$	–	–	3 [3]	3 [3]

Table 3. Cluster scaling relation assumptions and their labelling. Fiducial values are given first, followed by priors assumed in parameter estimation below (usually in brackets). Note that the colour coding at the top of the table is used to indicate these fiducial models throughout. See Sects. 3.2 & 3.3 and the Appendix for details.

Quantity	Labels/assumptions	
Redshift z	Realistic $\sigma(z)/(1+z) = 0.05$ 5% catastrophic (syst.)	Worst – case $\sigma(z)/(1+z) = 0.10$ 10% catastrophic (syst.)
	Realistic XSPEC-simulated XMM–Newton errors	Worst – case $\sigma(T) = 3 \times \sigma(T)_{\text{Realistic}}$
X-ray temperature T		

Table 4. Summary of measurement error assumptions and their labelling. See Sects. 3.4 & 3.5 and the Appendix for details.

are mainly interested in the shape and size of contours, or wish to separate possible biases from such an offset. This methodology is explained and motivated in detail in Appendix A2. As stated above, Fig. 6 compares constraints derived using this method to constraints derived from a Poisson sample of mock catalogues. The results confirm that constraints derived using our methodology provide an excellent estimate of the expected constraints. Note that in future real data analyses this methodology cannot be used, and there will in general be some offset.

The exploration of the likelihood function in parameter space was carried out using a custom code based on standard Monte Carlo Markov Chain techniques (Gelman & Rubin 1992; Gilks, Richardson & Spiegelhalter 1996; Lewis & Bridle 2002; Verde et al. 2003; Tegmark et al. 2004a; Dunkley et al. 2005). The calculation of the integrals involved in the likelihood was done with

the state-of-the-art numerical integration packages CUBPACK (Cools & Haegemans 2003) and CUBA (Hahn 2005).

5 RESULTS

5.1 Labelling

Generally, the colouring scheme in Table 3 will be used to indicate the fiducial cluster scaling relation model; see Sects. 3.2 and 3.3 as well as the Appendix. X-ray temperature and redshift errors will be indicated as ‘realistic’ or ‘worst-case’ according to Table 4; see Sects. 3.4 and 3.5 as well as the Appendix.

5.2 Expected cluster distributions

5.2.1 Without measurement errors

The expected 2D (T, z) distributions of clusters for our four standard models are shown in Fig. 7a (underlying distributions), Fig. 7b (expected detections) and Fig. 7c (detection efficiency), where the selection function has been used to go from Fig. 7a to Fig. 7b. The expected redshift distributions and total cluster number counts are shown similarly in Fig. 8. Note that as the $L-T$ relation changes, so does the expected number of detected clusters, since we are more likely to detect a cluster the more luminous it is (and for a given temperature, the cluster luminosity increases with redshift

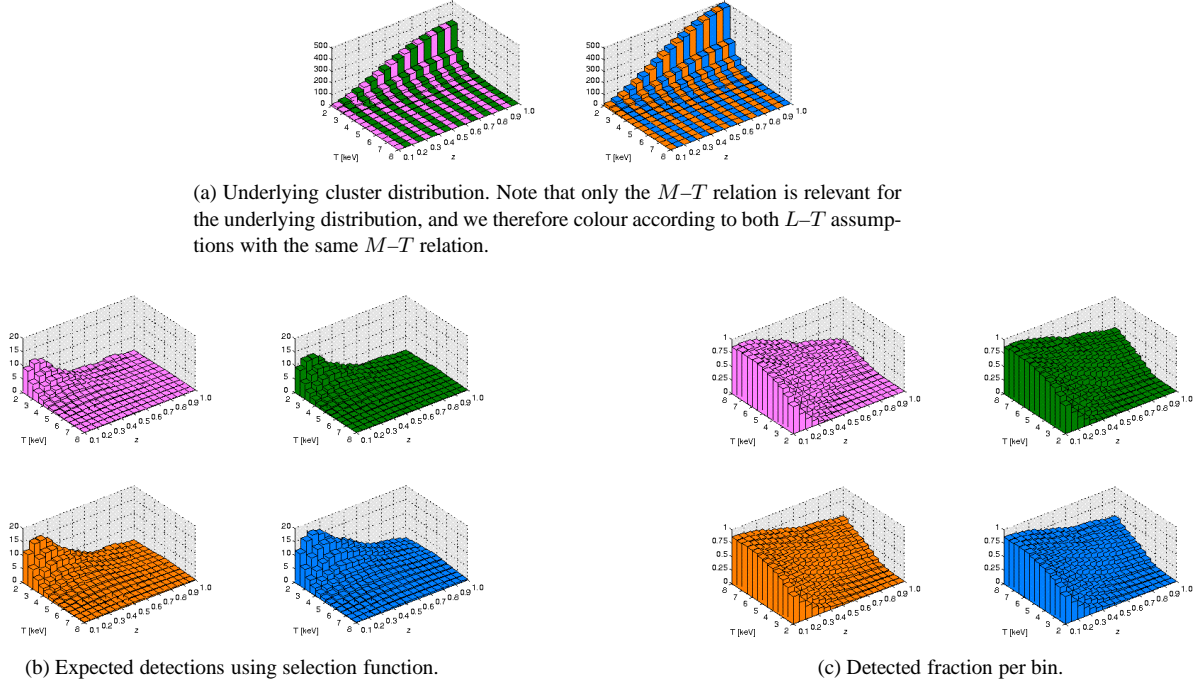


Figure 7. Expected cluster number count distributions for ^{500}XCS , for no $L-T$ nor $M-T$ scatter and no $L-T$ evolution (pink), no $L-T$ nor $M-T$ scatter and self-similar $L-T$ evolution (green), $L-T$ and $M-T$ scatter and no $L-T$ evolution (orange), and $L-T$ and $M-T$ scatter and self-similar $L-T$ evolution (blue). Bin sizes are $\Delta z = 0.05$ and $\Delta T = 0.5$ keV.

for self-similar $L-T$ evolution). The underlying distribution however is of course not dependent on the $L-T$ relation. We find that ^{500}XCS can be expected to find somewhere in the range of 250–700 clusters for its projected area of 500 deg^2 and $0.1 \leq z \leq 1.0$, $2 \text{ keV} \leq T \leq 8 \text{ keV}$. This corresponds to around 20 per cent of the 1500–3300 total number of clusters we would expect to detect with no photon count cut-off (effectively a ~ 50 -photon cut-off). This full set of XCS clusters will constitute a significant sample (relative to previous studies), representing around a quarter to a third of the actual 7000–10000 clusters present in the observed fields. Going to higher redshifts, we roughly estimate that a minimum of 250 clusters will be found at $z > 1$, of which at least 10 should have > 500 photons.

The XCS DR1 currently covers an area of 132 deg^2 , for which 125 clusters/groups with measured redshifts and > 500 photons have been identified from 164 candidate extended sources (with > 500 photon counts). No temperature, redshift or other cuts have been applied to this set. In the current redshift sample of 125 clusters with more than 500 photons, approximately 40 per cent have temperatures below 2 keV and are therefore classified as groups. We therefore expect the final number of genuine $T > 2 \text{ keV}$ clusters we detect in this area to be in the range 75–100, depending on the fraction of ‘extended’ sources detected by the survey that turn out not to be clusters (blended point sources, etc.). We have here assumed that selection effects in the redshift follow-up do not significantly bias this number. For our fiducial cosmology, we find that the corresponding expected number of clusters is 80–235, the range corresponding to the lower and upper limits from our set of scaling-relation assumptions. These two ranges are clearly consistent. The lower predicted limit corresponds to no $L-T$ evolution, and hence – all else equal – the observational result might indicate a near-constant $L-T$ relation.

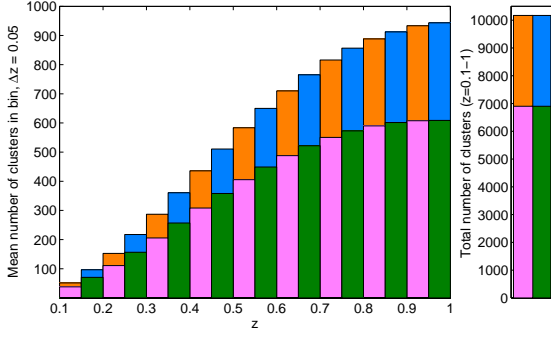
An overview of the expected observational limits of the

^{500}XCS for mass, X-ray temperature, X-ray luminosity and X-ray flux (in the $[0.1, 2.4] \text{ keV}$ band), is given in Fig. 9. We have there defined the detection limit, through the selection function, as $P(\text{detection}) \geq 0.5$. These limits are thus the values above which we expect to detect, with a photon count of 500 or above, at least half of the clusters. It is worth noting that the change in detection probability is slow as a function of X-ray temperature, and hence the concept of e.g. a single flux limit (which would correspond to a sharp transition between one and zero in the probability) is not suitable for defining the XCS sample. The underlying reason for this is that the *XMM* archive images occupy a range of different exposure times, hence individual flux limits. Caution is therefore advised when comparing Fig. 9 to similar plots based on a single flux or mass limit. For comparison, using $P(\text{detection}) \geq 0.05$ to define the detection limit leads to a flux limit of $\sim 5 \times 10^{-14} \text{ erg s}^{-1} \text{ cm}^{-2}$, considerably lower than that shown in Fig. 9.

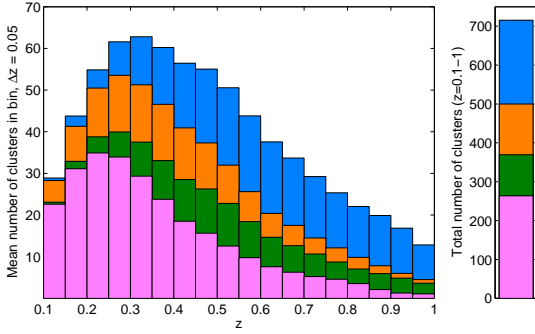
5.2.2 With measurement errors

Introducing measurement errors for redshift and X-ray temperature will introduce scattering of clusters across the redshift and temperature cut-offs. As the cluster distribution is not symmetric with respect to these cut-offs, there may be a net increase/decrease in the expected number of clusters as a result (a type of Malmquist bias). Furthermore, the measurement error distributions may also be asymmetric, as is our temperature error distribution. Note that the relevant ‘underlying’ cluster distributions for these purposes are the expected detections, shown in Fig. 7b.

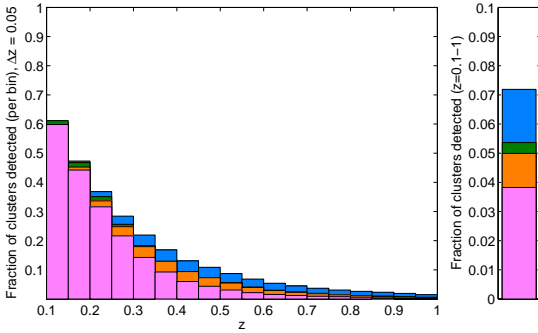
The change in the expected total number of clusters as a result of different measurement error assumptions are shown in Fig. 10. We find that the effect of measurement errors on the number count is significantly less than the effect of intrinsic scaling-relation scat-



(a) Underlying cluster distribution. Note that only the M - T relation is relevant for the underlying distribution, and we therefore colour according to both L - T assumptions with the same M - T relation.



(b) Expected detections using selection function.



(c) Detected fraction of clusters per bin.

Figure 8. Expected cluster distributions for the ^{500}XCS , for our four different cluster scaling relation cases.

ter (cf. Fig. 8b). This is not surprising since the scaling-relation scatter is based on the true underlying cluster distribution in Fig. 7a, a much steeper function than the expected detections in Fig. 7b.

We also see that only in the case of worst-case temperature errors is the Malmquist bias significant, and as we shall see later only in this case do the measurement errors give a significant bias in cosmological constraints, if unaccounted for. For realistic temperature errors, a net increase in clusters is seen, as the skewness of the temperature error distribution toward low temperatures (Fig. 4) is compensated by the somewhat larger number of low-temperature clusters scattering up in temperature at the low-temperature end. For worst-case temperature errors the temperature is very poorly constrained, and this compensatory effect is not sufficient to coun-

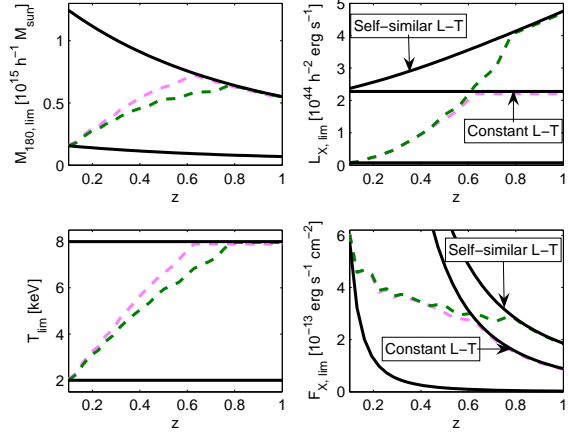


Figure 9. Expected observational limits for the ^{500}XCS (defined as $P(\text{detection}) \geq 0.5$), for the simplest case of no scatter in the cluster scaling relations and a constant (pink dashed line) or self-similar (green dashed line) L - T relation. Solid lines correspond to the hard temperature cut $2 \text{ keV} \leq T \leq 8 \text{ keV}$.

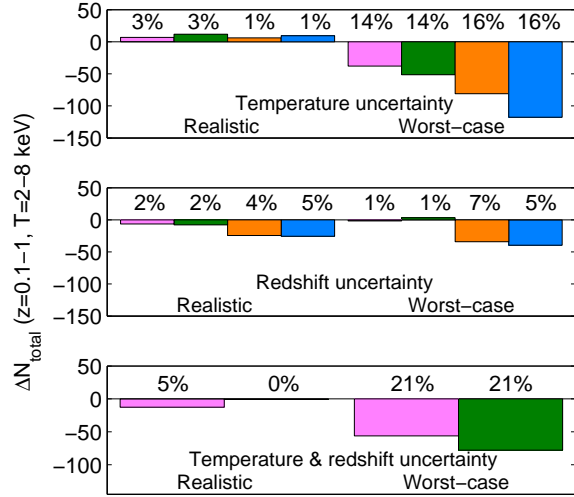


Figure 10. Changes in total number of clusters due to our different error assumptions, compared to no-errors distributions in Fig. 8b.

teract the net decrease in number of clusters. Redshift errors tend to cause a loss of clusters at the low-redshift end, as the smaller cosmic volume at lower redshifts means more clusters scatter down in redshift than scatter up. However, the redshift errors also affect the temperature determination, so that low-temperature clusters scattering up could give a net increase. For realistic redshift errors the size of this induced error in temperature is 5 per cent, which is too small to have a significant impact. For worst-case redshift errors, we see that for the case with no scaling-relation scatter, the induced temperature error of 10 per cent reduces the loss of clusters compared to that for realistic redshift errors. For the case with scaling-relation scatter, this effect is not significant, presumably due to the much sharper drop in cluster numbers at low redshifts seen for these models (Fig. 8b), leading to the direct redshift error dominating.

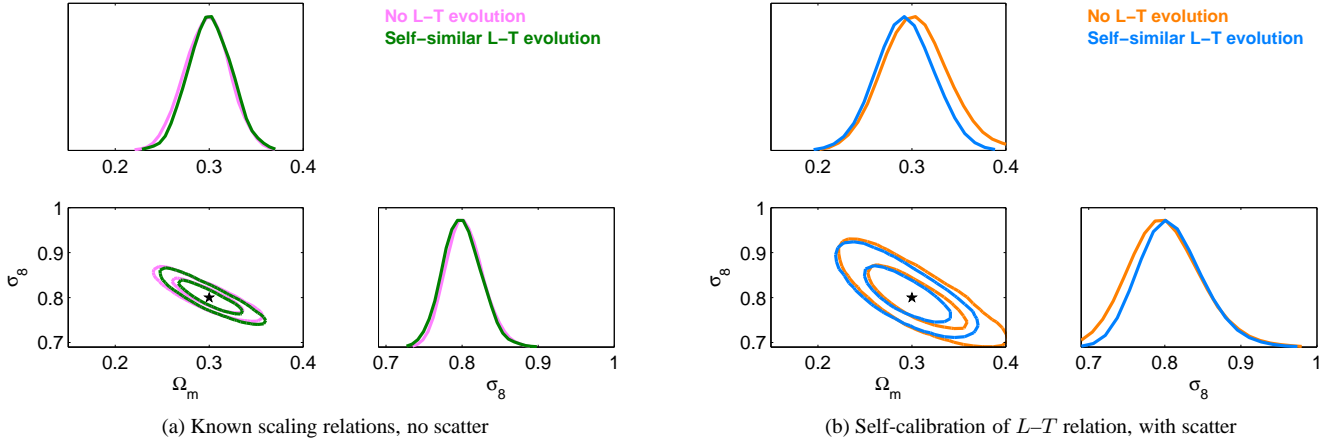


Figure 11. Expected 68 and 95 per cent parameter constraints for ^{500}XCS , without measurement errors. Stars denote the fiducial model assumed.

The fractional change in the number of clusters is very similar for the case with scaling-relation scatter as without such scatter. Hence, for the case with scatter, the statistical effect will tend to be larger since the difference to the N_{ideal} clusters with no measurement errors relative to the Poisson error bars,

$$\frac{\delta N_{\text{ideal}}}{\sigma((1+\delta)N_{\text{ideal}})} = \frac{\delta}{\sqrt{(1+\delta)}} \sqrt{N_{\text{ideal}}}, \quad (13)$$

grows with the number of clusters (and scatter increases the number). Here, δ is the fractional change in the number of clusters. Based on this, we estimate that for all the models we consider, an upper limit on the fractional change in cluster count for a less than 1σ (2σ) bias in constraints is around 4 (8) per cent, which compares favourably with the results for realistic errors in Fig. 10. (This comparison could be made more rigorous using the Kolmogorov–Smirnov test as in Haiman et al. (2001), but this treatment is sufficient for our purposes.) Due to computational limitations we have not calculated the change in number count for the case with scaling-relation scatter and both types of measurement errors, but based on the results obtained would expect them to be very similar (in fractional terms) to the results for the no-scatter case.

5.3 Constraints: without measurement errors

5.3.1 Known scaling relations, no scatter

For both choices of L - T relation (constant and self-similar), the expected constraints are shown in Fig. 11a. We expect ^{500}XCS to measure $\Omega_m = 0.3 \pm 0.02$, $\sigma_8 = 0.8 \pm 0.02$ in each case. The σ_8 - Ω_m degeneracy differs somewhat between the two L - T cases, for a constant L - T approximately given by

$$\sigma_8 = 0.8 \left(\frac{\Omega_m}{0.3} \right)^{-0.36}, \quad (14)$$

and for a self-similar L - T by

$$\sigma_8 = 0.8 \left(\frac{\Omega_m}{0.3} \right)^{-0.40}. \quad (15)$$

These degeneracies are somewhat different from previous studies, e.g. $\sigma_8 \propto \Omega_m^{-0.47}$ in Viana & Liddle (1999). That study however used only the total number of clusters above a certain temperature threshold to arrive at constraints. The orientation also depends

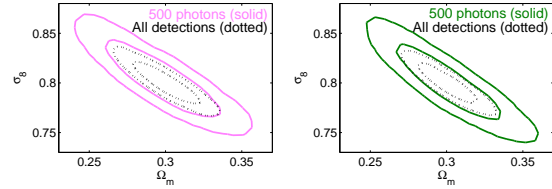


Figure 12. Comparison of ^{500}XCS to the case where all detections are used. A constant (left) or self-similar (right) L - T relation, and no L - T or M - T scatter was assumed. Contours correspond to 68 and 95 per cent confidence levels.

on redshift depth (Levine et al. 2002). These constraints are better than what has been forecast for XMM -LSS (Refregier et al. 2002), but the comparison is not entirely like-for-like as they employ the Press–Schechter mass function and assume a rather different fiducial σ_8 and Γ . The constraints are also fairly competitive with what can be expected from other surveys using e.g. the South Pole Telescope (SPT), *Planck* or *DUET* (Majumdar & Mohr 2004; Geisbüsch & Hobson 2007), but in making this comparison one should note that we employ much more restrictive priors; the set of free parameters is not exactly the same.

The constraints in Fig. 11a are for a photon-count threshold of 500. Lowering the photon-count threshold so that more clusters are included in the sample should clearly affect the size of constraints. We find that using all detections (corresponding to an effective photon-count threshold of typically ~ 50 photons) improves 1D constraints by about 40 per cent (Fig. 12). This corresponds to an increase in the number of clusters used of around 1200–1700 (400–500 per cent). For clusters with few photon counts the temperature errors will become very large (Liddle et al. 2001). Contamination from e.g. galaxy groups will also rise sharply with decreasing photon-count threshold, partly because clusters with low photon count will tend to have a low temperature. Hence, these estimates provide only upper limits on the possible constraint improvement. Taking error and contamination effects into account, it is likely that there would be only a weak improvement by including those XCS clusters expected to have a photon count below 500. However, follow-up observations with e.g. *XMM* or *IXO* (formerly *XEUS*) could improve the photon statistics of those clusters enough

L - T evolution		Known scaling relations, no scatter	Self-calibration of L - T , with scatter
Constant	Ω_m	0.30 ± 0.02	0.30 ± 0.03
	σ_8	0.80 ± 0.02	0.80 ± 0.05
	$\sigma_{\log L_X}$	–	$[0.2, 0.4]$
	α	–	-1.91 ± 0.12
	β	–	2.50 ± 0.33
	γ_z	–	$[-1, 1.5]$
Self-similar	Ω_m	0.30 ± 0.02	0.30 ± 0.03
	σ_8	0.80 ± 0.02	0.80 ± 0.04
	$\sigma_{\log L_X}$	–	$[0.2, 0.4]$
	α	–	-1.92 ± 0.12
	β	–	2.55 ± 0.31
	γ_z	–	$[-1, 1.5]$

Table 5. Expected 1σ parameter constraints for ^{500}XCS when marginalized over all other parameters, without measurement errors.

to make their inclusion in the analysis worthwhile. We discuss this in more detail in Sect. 6.

5.3.2 Self-calibration of L - T relation, with scatter

Self-calibration is the process by which e.g. the L - T relation can be constrained jointly with cosmological parameters using only the (T, z) cluster number counts (Hu 2003; Lima & Hu 2004; Majumdar & Mohr 2004; Lima & Hu 2005).

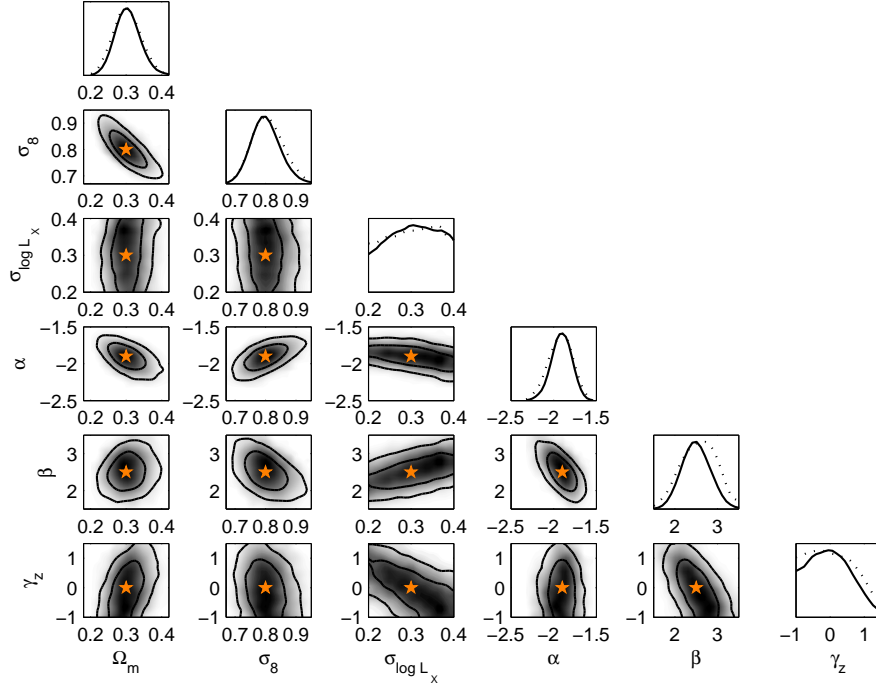
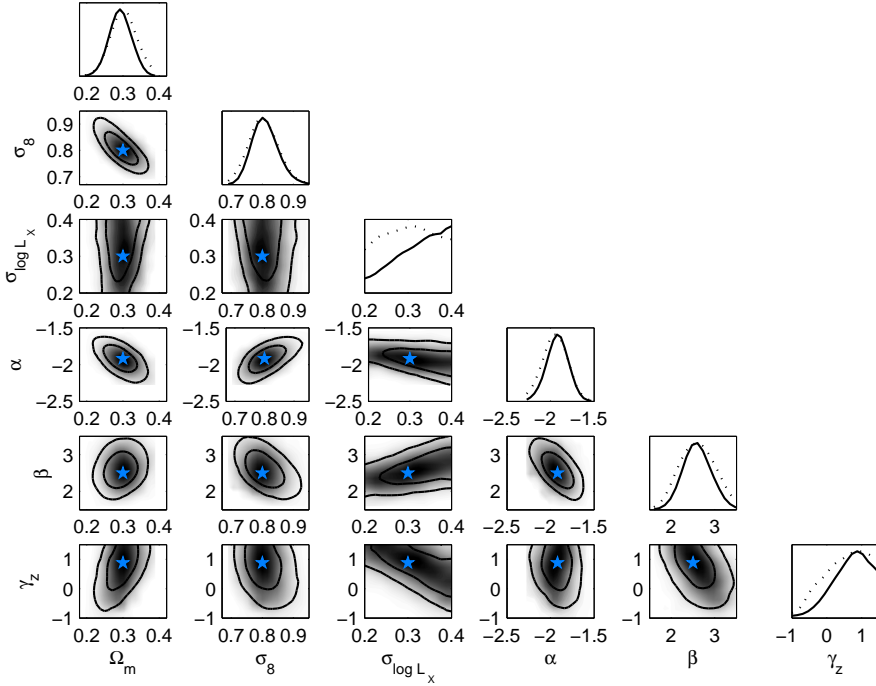
We find that jointly fitting for the cosmological parameters and the L - T relation, ^{500}XCS will measure $\Omega_m = 0.3 \pm 0.03$, $\sigma_8 = 0.8 \pm 0.05$ under our assumptions. The marginalized Ω_m - σ_8 likelihood distributions are shown in Fig. 11b, and the full set of likelihood distributions in Fig. 13 (note that Fig. 11b is just the top triangles of these plots). The 1D parameter constraints are listed in Table 5. The constraints for the case of self-similar L - T evolution appear narrower than for a constant L - T . This is due to the redshift-evolution prior, explained below, significantly cutting the distribution. We thus believe the constant L - T case to be most representative of the constraints we can expect. As expected, the constraints on Ω_m and σ_8 degrade when marginalizing over the four L - T parameters (compared to Fig. 11a), but still remain relatively small. In comparison to the South Pole Telescope, *Planck*, and *DUET* (Majumdar & Mohr 2004; Geisbüsch & Hobson 2007), our constraints are still competitive (we lack comparable results for *XMM*-LSS, but expect to do better given our larger survey area and depth). However, if we were to consider self-calibration of the M - T relation as well (rather than using an external description, as described in Sect. 3.2), those surveys would have more power than the XCS (using only archival *XMM* data) through the use of the cluster power spectrum (Majumdar & Mohr 2004; Lima & Hu 2004). In fact, we do not expect XCS to have any significant constraining power if the M - T relation is self-calibrated as well. We show examples of the effects of M - T systematics in Sect. 5.5. It has been shown (e.g. Majumdar & Mohr 2004) that small follow-up samples can dramatically improve the situation. Therefore, weak-lensing/SZ follow-up and/or a contiguous e.g. *XMM* survey would be highly advantageous (see also Bergé et al. 2008; Pierre et al. 2008). Comparing to Fig. 11a, although we lose constraining power due to an increase in the number of parameters, since we are including scaling-relation scatter the number of clusters increases significantly which mitigates the degradation. Note that, as shown in Table 3, we fit the data to a power-law L - T relation $\sim (1+z)^{\gamma_z}$. Although the functional form for a self-similar L - T used to gener-

ate data is different in principle, we have checked that a power law can approximate its redshift evolution very well.

Using (T, z) number-count self-calibration, based only on archival *XMM* data (Fig. 13), we can constrain the L - T normalization α to ± 0.12 (or ± 6 per cent) and the L - T slope β to $\sim \pm 0.3$ (or ± 13 per cent). The self-calibration procedure is not able to jointly constrain the scatter $\sigma_{\log L_X}$ and redshift evolution γ_z significantly. We have therefore imposed flat priors on these parameters, $0.2 \leq \sigma_{\log L_X} \leq 0.4$ and $-1 \leq \gamma_z \leq 1.5$ to limit the distribution within reasonable bounds of a size reflecting the minimum accuracy to which we would hope to measure these parameters from our direct L - T data, i.e. also taking into account the measured X-ray flux (see also Table 3).

Thus, the self-calibration power to constrain the L - T relation is present in the data, but as can be seen in Fig. 13 there are strong degeneracies between parameters. The main degeneracy is that between γ_z and $\sigma_{\log L_X}$; increasing $\sigma_{\log L_X}$ can easily be offset by reducing γ_z , which also is easy to understand physically as they both effectively scale the cluster luminosities up or down, and corresponds to the observation by several authors (e.g. Branchesi et al. 2007; Maughan 2007; Nord et al. 2008; Pacaud et al. 2007) that L - T scatter can mimic L - T evolution (also discussed in Sect. 3.3.1). The redshift evolution γ_z is also degenerate with the L - T slope β , which is thus itself degenerate with $\sigma_{\log L_X}$. Interestingly though, the cosmological parameters show little degeneracy with $\sigma_{\log L_X}$. It is the result of these degeneracies that all four L - T parameters cannot be jointly constrained. Bayesian Complexity (Kunz, Trotta & Parkinson 2006) suggests that at most five parameters (including Ω_m and σ_8) can be fully constrained, which is also what we find in practice. As one might expect, we will therefore have to rely on our direct L - T measurement to constrain the L - T scatter and evolution (as proposed by Verde, Haiman & Spergel 2002; Hu 2003; Battye & Weller 2003; Wang et al. 2004; Lima & Hu 2005).

The fact that our relatively generous priors on the L - T scatter and evolution still restricts the distribution, affecting the size of cosmological constraints, also serves to illustrate a slightly different point of view: turning the problem around, and using complementary cosmological data to constrain e.g. Ω_m and σ_8 , thereby possibly also improving constraints on astrophysical parameters (as noted by e.g. Levine et al. 2002; Hu & Kravtsov 2003; Hu 2003).

(a) Constant L - T relation

(b) Self-similar L - T relation. (As can be surmised from some of the 1D distributions, the marginalized and mean likelihoods approach each other very slowly in the MCMC due to the prior cutting the distribution, however the statistical properties of the distribution have converged appropriately.)

Figure 13. Expected 68 and 95 per cent parameter constraints for ^{500}XCS , with scaling-relation scatter and no measurement errors, and fitting jointly with L - T relation (self-calibration) for which reasonable priors on scatter and redshift evolution have been adopted. Solid lines correspond to marginalized likelihood, dotted lines and shading to mean likelihood. Stars denote the fiducial model assumed.

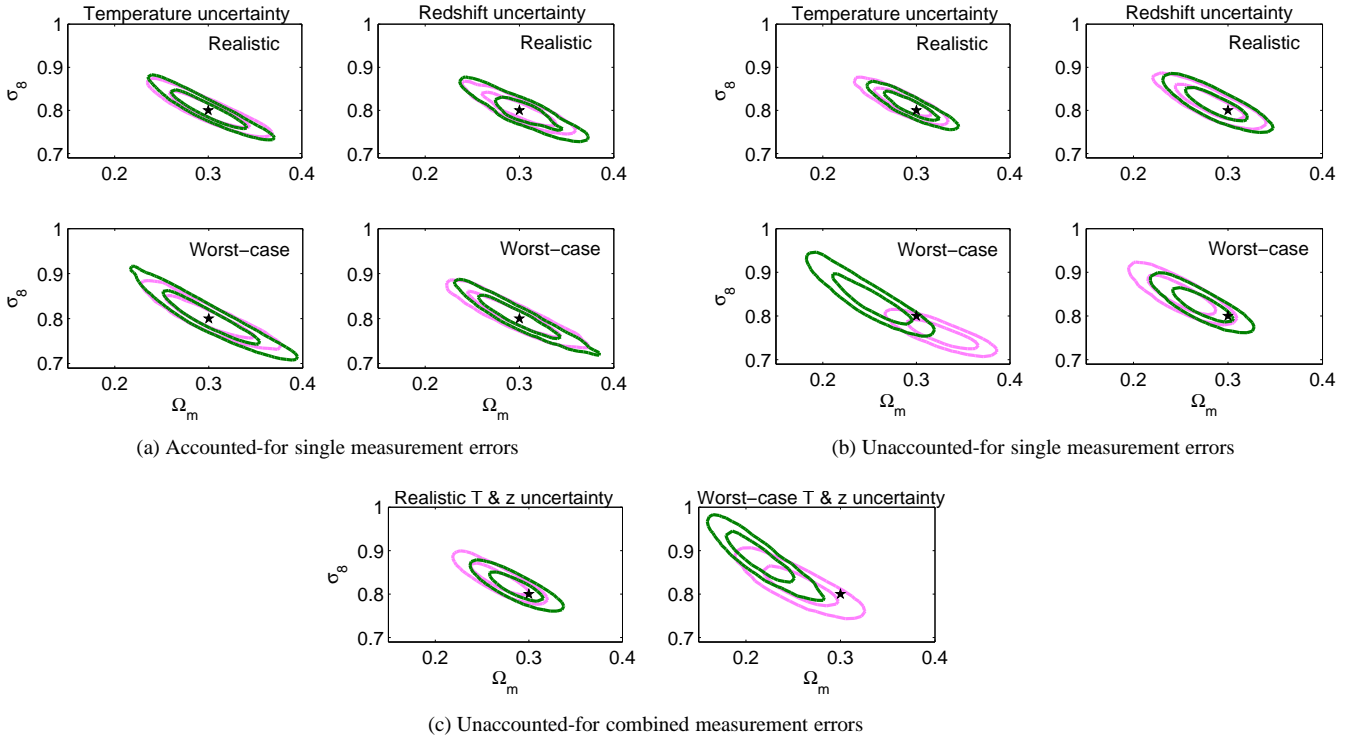


Figure 14. Expected 68 and 95 per cent parameter constraints for ^{500}XCS , for known scaling relations, no scatter, and with measurement errors. Stars denote the fiducial model assumed.

L - T evolution		Realistic T errors	Worst-case T errors	Realistic z errors	Worst-case z errors
Constant	Ω_m	0.30 ± 0.03	0.30 ± 0.03	0.30 ± 0.02	0.30 ± 0.03
	σ_8	0.80 ± 0.03	0.80 ± 0.03	0.80 ± 0.02	0.80 ± 0.03
Self-similar	Ω_m	0.30 ± 0.03	0.30 ± 0.03	0.30 ± 0.03	0.30 ± 0.03
	σ_8	0.80 ± 0.03	0.80 ± 0.04	0.80 ± 0.03	0.80 ± 0.03

Table 6. Expected 1σ parameter constraints for ^{500}XCS when marginalized over the other parameter, for known scaling relations, no scatter, and with accounted-for measurement errors.

5.4 Constraints: with measurement errors

5.4.1 Known scaling relations, no scatter

The effect on derived cosmological constraints from measurement errors in X-ray temperature and redshift is small. Taking into account knowledge of the error distributions in the data analysis, we find that the size of uncertainties increases somewhat compared to the no-errors case (see Fig. 14a and Table 6, cf. Fig. 11a and column 1 in Table 5). Interestingly, even with temperature or redshift errors of an unrealistically large magnitude, the effect on the constraints is small. As such, we expect the broadening of constraints due to measurement errors to be a minor effect compared to the effects of possible systematic errors. These findings are in agreement with what has already been found by e.g. Huterer et al. (2004, 2006); Lima & Hu (2007).

The effect of ignoring temperature and redshift errors in the fitting procedure can to some extent model one such systematic; poor knowledge of the measurement error distributions. As can be seen in Fig. 14b, we find that when ignoring measurement errors in the fitting, for all combinations of single measurement errors (i.e. only z or T at a time), the difference in cosmological con-

straints compared to the fiducial model is within 2σ (and most are within 1σ). For combined z and T measurement errors, the same is still true for realistic errors, but for a self-similar L - T and worst-case errors the bias is larger than 2σ (see Fig. 14c). These results agree well with the expectations presented in Sect. 5.2.2, and thus suggest that a good estimate of the bias in cosmological constraints due to Malmquist-bias effects can be obtained by comparing the net Malmquist bias to the Poisson error of the total cluster number count (at least to roughly discriminate $> 2\sigma$ bias from $< 2\sigma$ bias). This is not that surprising as the shape of the cluster distribution does not differ much between such models, and thus the total number count carries most of the information (also noted in Haiman et al. 2001). The 1D constraints corresponding to Figs. 14b & 14c are listed in Table 7.

5.4.2 Self-calibration of L - T relation, with scatter

Because of computational limitations we have not explicitly calculated cosmological constraints for self-calibration with measurement errors. We have however checked that when scatter is included in the data, the effect of temperature and redshift errors on

L - T evolution		Realistic T errors	Worst-case T errors	Realistic z errors	Worst-case z errors	Realistic T & z errors	Worst-case T & z errors
Constant	Ω_m	0.28 ± 0.02	0.33 ± 0.02	0.28 ± 0.02	0.25 ± 0.02	0.27 ± 0.02	0.26 ± 0.03
	σ_8	0.82 ± 0.02	0.76 ± 0.02	0.82 ± 0.03	0.85 ± 0.03	0.83 ± 0.02	0.82 ± 0.03
Self-similar	Ω_m	0.29 ± 0.02	0.25 ± 0.03	0.29 ± 0.02	0.27 ± 0.02	0.29 ± 0.02	0.22 ± 0.02
	σ_8	0.81 ± 0.02	0.84 ± 0.04	0.81 ± 0.03	0.83 ± 0.03	0.82 ± 0.02	0.88 ± 0.04

Table 7. Expected 1σ parameter constraints for ^{500}XCS when marginalized over the other parameter, for known scaling relations, no scatter, and with unaccounted-for measurement errors.

	1	2	3	4	5	6
Ω_m	0.35 ± 0.03	0.23 ± 0.02	0.25 ± 0.01	0.30 ± 0.01	0.31 ± 0.02	0.23 ± 0.01
σ_8	0.71 ± 0.02	0.93 ± 0.02	0.96 ± 0.02	0.90 ± 0.02	0.83 ± 0.02	1.08 ± 0.02

Table 8. Expected 1σ parameter constraints for ^{500}XCS when marginalized over the other parameter, for systematic errors in the scaling-relation assumptions (Fig. 15). The different scenarios are numbered according to the order in which they are listed in Fig. 15.

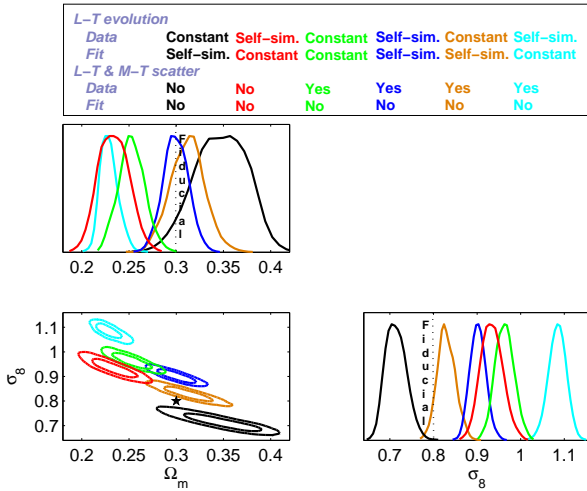


Figure 15. Expected 68 and 95 per cent parameter constraints from the ^{500}XCS , for various cluster scaling relation assumptions inconsistent with the fiducial model used for generating the data. The different data and fitting assumptions are colour coordinated with the contours, and listed in the panel above the plot. The model parameters are the same as previously, and listed in Table 3. The corresponding cluster distributions in redshift and temperature can be found in Fig. 7b.

the expected cluster distribution is very similar to the case where no scatter is included, see Fig. 10, and the discussion in the preceding Section and Sect. 5.2.2. We thus expect that the effect from measurement errors on constraints where scatter is included, with or without self-calibration, can be expected to be small or negligible – both in terms of bias if the errors are ignored, or broadening of error contours when errors are taken into account. We therefore believe that the self-calibration results for the case without measurement errors (Figs. 11b & 13, Table 5) should provide a good rough approximation of the expected self-calibration constraints with measurement errors. Note that this situation is bound to change once direct L - T data is added to the procedure, as the temperature errors will then have a significant impact on the accuracy to which the evolution of the L - T relation can be determined, hence setting the size of the constraints on $\sigma_{\log L_X}$ and γ_z . One can therefore *not* conclude that temperature errors are largely unimportant for

the cosmological constraints we will ultimately produce from the data, but an upper limit on the size is set by this work (see e.g. Verde et al. 2002; Hu 2003; Battye & Weller 2003).

5.5 Constraints: systematic biases

It is clear from the above sections that measurement errors in the guises we consider are not expected to be a major source of bias or degradation of constraints vis-à-vis the underlying cluster distribution. However, if incorrect assumptions as to the characteristics of the M - T and L - T relations are used when fitting the data, significant bias may occur, as seen in Figs. 15 & 16 and Tables 8 & 9.

Looking first at Fig. 15 (and Table 8 for the 1D marginalized constraints), the figure shows how both the size and best-fitting values of cosmological constraints are affected when ignoring scatter in the scaling relations, using an inappropriate L - T relation, or both. The first case (from left in the panel above the plot) shows how using a self-similar L - T to fit data coming from a constant L - T leads to an overestimation of Ω_m . Comparing the second, third and fourth cases, we can see that L - T evolution and scaling-relation scatter all have a similar effect when unaccounted for, all leading to an overestimation of σ_8 (and consequently underestimation of Ω_m). As they both have a similar effect, the self-similar evolution in the fifth case can mimic some of the unaccounted-for scatter, leading to a lesser overestimation than for the previous cases. On the other hand, the sixth and last case combines the two effects thus leading to a dramatic overestimation of σ_8 . As such, this last case represents a worst-case scenario for this type of bias.

The other figure, Fig. 16 (and Table 9 for the 1D marginalized constraints), shows how constraint size and best-fitting values vary with systematic errors in the M - T relation only. The first two cases (from left in the panel above the plot) illustrate significantly underestimating a scatter of 10 or 15 per cent (deviations similar to what might be expected according to Vikhlinin 2006). This leads to an overestimation of σ_8 , and relatively narrow constraints, since scatter significantly increases the number of detected clusters. The largest impact seen in this figure comes from poor knowledge of the redshift evolution of the M - T relation, seen in the second pair of contours. We consider a self-similar M - T analyzed as constant in redshift, and a constant M - T analyzed as self-similar. In both cases the deviation from the fiducial model is very significant, with the size of constraints also affected, due to the fiducial-model as-

	1	2	3	4	5	6
Ω_m	0.245 ± 0.005	0.253 ± 0.008	0.47 ± 0.05	0.20 ± 0.01	0.34 ± 0.02	0.24 ± 0.03
σ_8	0.878 ± 0.007	0.87 ± 0.01	0.59 ± 0.03	1.04 ± 0.02	0.87 ± 0.03	0.72 ± 0.04

Table 9. Expected 1σ parameter constraints for ^{500}XCS when marginalized over the other parameter, for systematic errors in the M – T relation assumptions (Fig. 16). The different scenarios are numbered according to the order in which they are listed in Fig. 16.

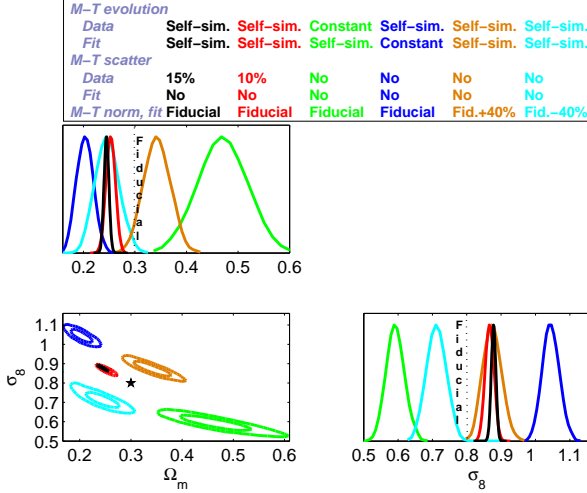


Figure 16. Expected 68 and 95 per cent parameter constraints from the ^{500}XCS , for various mass–temperature–relation assumptions inconsistent with the fiducial model used for generating the data. The different data and fitting assumptions are colour coordinated with the contours, and listed in the panel above the plot. Throughout, a self-similar L – T relation with scatter (as specified in Table 3) has been assumed.

sumptions having a significant impact on the number of detected clusters. The third, and last, pair of contours show the effect of over- or underestimating the normalization mass by 40% (this value agrees with what might be expected according to e.g. Vikhlinin 2006). Overestimation of the mass leads to an overestimation of σ_8 , since the higher the assumed mass for a given temperature, the fewer the number of clusters at that temperature. Underestimation of the mass consequently also leads to an underestimation of σ_8 .

In most cases, the constraints are more than 3σ away from the fiducial model. Referring back to the discussion on Poisson errors in Sect. 5.2.2 and applying that to the relevant cluster distributions (see Fig. 8b), this result is not surprising. We find that in terms of total number count Poisson error bars, the discrepancy between data and fitting assumptions are at least $\sim 6\sigma$. These limitations will apply to any galaxy cluster survey employing cluster scaling relations to arrive at results, certainly all X-ray surveys, with the exact susceptibility to bias given by the combination of true cluster distribution and survey selection function. This stresses the importance of knowledge of the behaviour of the scaling relations in the form of self-calibration and/or separate follow-up information. For this, accurate knowledge of the selection function is necessary, so that scaling-relation scatter and evolution can be correctly distinguished (as pointed out in e.g. Pacaud et al. 2007).

6 DISCUSSION AND CONCLUSIONS

6.1 The XCS forecast

The XMM Cluster Survey (XCS) will cover 500 deg^2 and is expected to produce one of the largest catalogues of galaxy clusters so far, with ~ 1500 – 3300 clusters having $0.1 \leq z \leq 1$, $2 \text{ keV} \leq T \leq 8 \text{ keV}$. Around 20 per cent of these will belong to the ^{500}XCS sample that have sufficient photons (> 500) for their X-ray temperature to be reliably estimated. In a rough approximation, we expect to find an additional 250 or more clusters at $z > 1$, of which at least 10 should have > 500 photons. We have proven the potential of the XCS with the recent discovery of the most distant galaxy cluster known, XMMXCS J2215.9-1738 at $z = 1.457$ (Stanford et al. 2006; Hilton et al. 2007). Cluster redshifts are obtained from both public-domain photometry and the NOAO–XCS Survey (NXS, Miller et al. 2006). To date, more than 400 XCS candidates have been optically confirmed. An initial observational area of 132 deg^2 (XCS DR1) contains in the range 75–100 detected clusters with $T > 2 \text{ keV}$ and > 500 photons. This number is consistent with the theoretical expectations presented here for our fiducial models.

We have shown the power in determining both cosmological and astrophysical parameters expected from the XMM archive, using only self-calibration from the (T, z) distribution and taking detailed selection function, cluster distribution and measurement error modeling into account in a Monte Carlo Markov Chain (MCMC) setting. Inclusion of the selection function requires the specification of the luminosity–temperature relation, and thus enables us to also self-calibrate this relation. We also introduce and motivate a new ‘smoothed Maximum Likelihood estimate’ of the expected constraints, which can be regarded as intermediate between a Fisher matrix analysis and a full mock catalogue ensemble averaging in MCMC.

We expect the ^{500}XCS to measure

$$\begin{aligned} \sigma(\Omega_m) &< 0.03 \quad (10\%), & \sigma(\alpha) &< 0.12 \quad (6\%), \\ \sigma(\sigma_8) &< 0.05 \quad (6\%), & \sigma(\beta) &< 0.33 \quad (13\%), \end{aligned}$$

for a flat Λ CDM Universe, the uncertainty on Ω_m also being that on Ω_Λ . The cosmological constraints are similar to those already obtained using gas mass fraction measurements (e.g. Allen et al. 2002, 2008). They are better than those that can be expected from XMM–LSS (Refregier et al. 2002), because XCS covers more area than XMM–LSS (predicted maximum area of 64 deg^2 , but so far results for only 5 deg^2 have been published) and has a higher average exposure time. Our constraints are also somewhat competitive compared to expected constraints from e.g. the SPT, Planck, and DUET (Majumdar & Mohr 2004; Geisbüsch & Hobson 2007), except if self-calibration of the mass–temperature relation is also considered. The scatter and redshift evolution of the luminosity–temperature relation cannot be jointly constrained to a significant degree by the self-calibration data alone; additional data – archival XMM and/or follow-up – is needed to distinguish e.g. no evolution from self-similar evolution if the scatter is left as a free parameter.

Like e.g. Levine et al. (2002); Hu & Kravtsov (2003); Hu (2003), we note that there is also potential to use this conversely, to let complementary cosmological data help constrain astrophysical parameters. We may return to this in future work.

6.2 Measurement errors

We include for the first time realistic temperature measurement errors, based on detailed XSPEC simulations of the *XMM* fields, and propagate redshift errors to the temperature determination. The presence of realistic or worst-case measurement errors in X-ray temperature and redshift will have only a small impact on the accuracy to which cosmological parameters can be expected to be measured, of order 0.01 in 1D confidence limits. Furthermore, we find that imperfect knowledge of the variances of measurement errors, or the presence of catastrophic photometric redshifts, should not produce significant bias in the cosmological constraints. We conclude that, under these assumptions, even ignoring the expected realistic measurement errors in the data analysis will provide a reasonable estimate of the true constraints. For the case where direct L – T data is included in the analysis, the impact of measurement errors (including susceptibility to systematics) will be larger (Verde et al. 2002; Hu 2003; Battye & Weller 2003). The size of constraints forecast here provide an upper limit for that scenario.

It is already known (Huterer et al. 2004, 2006; Lima & Hu 2007) that irreducible systematic errors in redshift estimation is a potential problem for cluster surveys, but we leave for future work the specific requirements for the XCS.

We do not yet take into account the variation of photon count with temperature/luminosity, and how that affects the size of temperature errors. Including this effect, instead of employing a lower threshold only, may well improve the size of our constraints. However the maximum improvement for self-calibration is small. For inclusion of direct L – T data the importance will be larger.

6.3 Cluster scaling relations

The choice of L – T relation itself has no significant impact on the size of cosmological constraints. In our considerations, we do not yet take into account the separate L – T measurement to be performed by the XCS. In the final data analysis, the L – T measurements will be jointly fitted with the cluster distribution. Hence, our expected constraints represent a worst-case scenario of no direct data on the L – T relation. We plan to revisit the issue of the XCS L – T measurement in the future. As an example, estimates for the *DUET* survey (Majumdar & Mohr 2004) show that follow-up information on the M – T relation can improve constraints by more than a factor of three.

We quantitatively show that making incorrect assumptions about the cluster scaling relations can typically result in at least a 2σ – 3σ bias in cosmological constraints, a result which can be considered generic for all X-ray and SZ cluster surveys, and those optical surveys relying on cluster scaling relations. Thus, parametrizing the scaling relations appropriately and using self-calibration and/or follow-up information is crucial to arrive at robust results. This places high demands on precise characterization of the survey selection function to accurately distinguish scaling-relation evolution and scatter. That is not a problem for X-ray cluster surveys (as they generally have the best-understood selection functions), and shows the importance of the XCS measurement of the L – T relation for cosmological applications. The *XMM*–LSS collaboration have already pointed this out, and obtained some first results (Pacaud et al.

2007). A potential pitfall however is the possible redshift evolution of the L – T scatter, as observed in the CLEF simulation (Kay et al. 2007). This has not so far been considered in the literature, but is a possible source of bias that should be better understood. The future *IXO* mission (Bleeker & Mendez 2002) will be of great importance for precision measurements of all details of the L – T relation. The XCS will provide thousands of clusters for *IXO* to target.

An important source of uncertainty is the mass–temperature relation. We have shown quantitatively that, as for the luminosity–temperature relation, imperfect knowledge can easily lead to significant bias. Joint estimation of the mass–temperature relation will lead to broader constraints, and we do not expect the XCS to be able to constrain both the L – T and M – T relations simultaneously. Generally, it has been found that an accuracy of less than 10 per cent in the M – T relation will be needed, and that self-calibration (particularly if making use of the power spectrum, which XCS can not do) and/or small follow-up samples can achieve that (Holder et al. 2001; Haiman et al. 2001; Levine et al. 2002; Majumdar & Mohr 2003, 2004; Wang et al. 2004; Lima & Hu 2004; Lima & Hu 2005). A recent development is the claim that the X-ray luminosity is a better mass proxy than previously thought (Maughan 2007). This remains somewhat controversial, but could be worthwhile to consider. Its potentially low scatter and the prospect of including low-temperature clusters, for which the temperature cannot be accurately measured, makes this interesting. Likewise, employing the quantity Y_X (e.g. Kravtsov et al. 2006) would also be an interesting option to consider. We leave the XCS-specific details for future work.

It has also been noted by, amongst others, Younger et al. (2006) and Ascasibar & Diego (2008), that the choice of parametrization for the cluster scaling relations can have a significant impact on the size of cosmological constraints, and they argue that a physically-motivated form is beneficial. As also noted by Lima & Hu (2007), efforts in correlating physical properties of clusters, such as that of Shaw et al. (2006), could therefore be of great importance for the size of cosmological constraints, not just biases or astrophysics. However, as the observed dependence on parametrization appears to largely come from an Ω_m – Ω_Λ degeneracy, and in this work we assume that $\Omega_\Lambda = 1 - \Omega_m$, we do not expect this to be of importance for our results here.

6.4 Selection function

The cluster model assumptions made in our calculation of the selection function could have an impact on cluster detectability and thus cosmological constraints. For this reason, we have studied the selection function dependence on cluster structure parameters (for the beta model assumed). For core radii within reasonable bounds, the relative difference compared to our standard beta model is of the order 10 per cent. This number is however an overestimation to the resulting overall uncertainty in cluster number predictions, as it does not include any detailed knowledge of the cluster population, in particular the detailed distribution of cluster-model parameters. Therefore, the significance is limited. We expect the real differences to be smaller. These results agree with those of Burenin et al. (2007) for the 400d survey, which show that reasonable variations in cluster size, morphology and scaling relations induce an uncertainty in the detectability for a given flux of typically less than 5 per cent. In a future, real analysis, the cluster-model parameter distribution would be included along with a selection function dependence on these parameters, thereby also significantly reducing any uncertainty. We are currently studying the selection function further

REFERENCES

- Allen S. W., Rapetti D. A., Schmidt R. W., Ebeling H., Morris R. G., Fabian A. C., 2008, *MNRAS*, 383, 879
- Allen S. W., Schmidt R. W., Fabian A. C., 2002, *MNRAS*, 334, L11
- Arnaud K., 1996, in Jacoby G., Barnes J., eds, *Astronomical Data Analysis Software and Systems V* Vol. 101 of ASP Conf. Series, Xspec: The first ten years. p. 17
- Arnaud M., 2005, in Melchiorri F., Rephaeli Y., eds, *Proc. Enrico Fermi International School of Physics Course CLIX* (arxiv:astro-ph/0508159)
- Arnaud M., Pointecouteau E., Pratt G. W., 2005, *A&A*, 441, 893
- Ascasibar Y., Diego J. M., 2008, *MNRAS*, 383, 369
- Bahcall N. A., Fan X., Cen R., 1997, *ApJ*, 485, L53+
- Bahcall N. A., Ostriker J. P., Perlmutter S., Steinhardt P. J., 1999, *Sci*, 284, 1481
- Balogh M. L., et al., 2006, *MNRAS*, 366, 624
- Bardeen J. M., Bond J. R., Kaiser N., Szalay A. S., 1986, *ApJ*, 304, 15
- Battye R. A., Weller J., 2003, *PRD*, 68, 083506
- Bergé J., et al., 2008, *MNRAS*, pp 218–
- Blake C., Collister A., Bridle S., Lahav O., 2007, *MNRAS*, 374, 1527
- Blanchard A., Sadat R., Bartlett J. G., Le Dour M., 2000, *A&A*, 362, 809
- Bleeker J., Mendez M., 2002, preprint (arXiv:astro-ph/0207283)
- Borgani S., et al., 2001, *ApJ*, 561, 13
- Borgani S., et al., 2004, *MNRAS*, 348, 1078
- Branchesi M., Gioia I. M., Fanti C., Fanti R., 2007, *A&A*, 472, 739
- Brodwin M., et al., 2007, *ApJ*, 671, L93
- Bryan G. L., Norman M. L., 1998, *ApJ*, 495, 80
- Burenin R. A., Vikhlinin A., Hornstrup A., Ebeling H., Quintana H., Mescheryakov A., 2007, *ApJS*, 172, 561
- Carlstrom J. E., Holder G. P., Reese E. D., 2002, *ARA&A*, 40, 643
- Collins C. A., et al., 2000, *MNRAS*, 319, 939
- Cools R., Haegemans A., 2003, *ACM Transactions on Mathematical Software*, 29, 287
- Donahue M., Voit G. M., 1999, *ApJ*, 523, L137
- Dunkley J., Bucher M., Ferreira P. G., Moodley K., Skordis C., 2005, *MNRAS*, 356, 925
- Eisenstein D. J., et al., 2005, *ApJ*, 633, 560
- Eisenstein D. J., Hu W., 1998, *ApJ*, 496, 605
- Eke V. R., Cole S., Frenk C. S., Patrick Henry J., 1998, *MNRAS*, 298, 1145
- Erlich J., Glover B., Weiner N., 2008, *Journal of Cosmology and Astro-Particle Physics*, 3, 6
- Ettori S., et al., 2004a, *MNRAS*, 354, 111
- Ettori S., et al., 2004b, *A&A*, 417, 13
- Ettori S., Tozzi P., Rosati P., 2003, *A&A*, 398, 879
- Evrard A. E., et al., 2002, *ApJ*, 573, 7
- Frenk C. S., White S. D. M., Efstathiou G., Davis M., 1990, *ApJ*, 351, 10
- Geisbüsch J., Hobson M. P., 2007, *MNRAS*, 382, 158
- Gelman A., Rubin D., 1992, *Statistical Science*, 7, 457
- Gilks W. R., Richardson S., Spiegelhalter D. J., eds, 1996, *Markov Chain Monte Carlo in Practice*. Chapman & Hall
- Gladders M. D., 2004, in Mulchaey J. S., Dressler A., Oemler A., eds, *Clusters of Galaxies: Probes of Cosmological Structure and Galaxy Evolution* Vol. 3 of Carnegie Observatories Astrophysics Series. Cambridge University Press, p. 89
- Gladders M. D., Yee H. K. C., 2000, *AJ*, 120, 2148
- Gladders M. D., Yee H. K. C., 2005, *ApJS*, 157, 1
- Gladders M. D., Yee H. K. C., Majumdar S., Barrientos L. F., Hoekstra H., Hall P. B., Infante L., 2007, *ApJ*, 655, 128
- Gonzalez A. H., Zaritsky D., Wechsler R. H., 2002, *ApJ*, 571, 129
- Hahn T., 2005, *Comp. Phys. Comm.*, 168, 78
- Haiman Z., et al., 2005, preprint (arXiv:astro-ph/0507013)
- Haiman Z., Mohr J. J., Holder G. P., 2001, *ApJ*, 553, 545
- Henry J. P., 1997, *ApJ*, 489, L1+
- Henry J. P., 2000, *ApJ*, 534, 565
- Henry J. P., 2004, *ApJ*, 609, 603
- Hicks A. K., et al., 2008, *ApJ*, 680, 1022
- Hilton M., et al., 2007, *ApJ*, 670, 1000
- Holden B. P., Stanford S. A., Squires G. K., Rosati P., Tozzi P., Eisenhardt P., Spinrad H., 2002, *AJ*, 124, 33
- Holder G., 2006, preprint (arXiv:astro-ph/0602251)
- Holder G., Haiman Z., Mohr J. J., 2001, *ApJ*, 560, L111
- Hsieh B. C., Yee H. K. C., Lin H., Gladders M. D., 2005, *ApJS*, 158, 161
- Hu W., 2003, *PRD*, 67, 081304
- Hu W., Cohn J. D., 2006, *PRD*, 73, 067301
- Hu W., Kravtsov A. V., 2003, *ApJ*, 584, 702
- Huterer D., Kim A., Krauss L. M., Broderick T., 2004, *ApJ*, 615, 595
- Huterer D., Takada M., Bernstein G., Jain B., 2006, *MNRAS*, 366, 101
- Huterer D., Turner M. S., 2001, *PRD*, 64, 123527
- Ikebe Y., Reiprich T. H., Böhringer H., Tanaka Y., Kitayama T., 2002, *A&A*, 383, 773
- Jahoda K., the DUET collaboration 2003, *Astronomische Nachrichten*, 324, 132
- Jenkins A., et al., 2001, *MNRAS*, 321, 372
- Juin J. B., Yvon D., Refregier A., Yèche C., 2005, preprint (arXiv:astro-ph/0512378)
- Kaiser N., 1986, *MNRAS*, 222, 323
- Kay S. T., da Silva A. C., Aghanim N., Blanchard A., Liddle A. R., Puget J.-L., Sadat R., Thomas P. A., 2007, *MNRAS*, 377, 317
- Klypin A., Macciò A. V., Mainini R., Bonometto S. A., 2003, *ApJ*, 599, 31
- Kotov O., Vikhlinin A., 2005, *ApJ*, 633, 781
- Kotov O., Vikhlinin A., 2006, *ApJ*, 641, 752
- Kravtsov A. V., Vikhlinin A., Nagai D., 2006, *ApJ*, 650, 128
- Kunz M., Trotta R., Parkinson D., 2006, *PRD*, 74, 023503
- Levine E. S., Schulz A. E., White M., 2002, *ApJ*, 577, 569
- Lewis A., Bridle S., 2002, *PRD*, 66, 103511
- Liddle A. R., Viana P. T. P., Romer A. K., Mann R. G., 2001, *MNRAS*, 325, 875
- Lima M., Hu W., 2004, *PRD*, 70, 043504
- Lima M., Hu W., 2005, *PRD*, 72, 043006
- Lima M., Hu W., 2007, *PRD*, 76, 123013
- Linder E. V., Jenkins A., 2003, *MNRAS*, 346, 573
- Łokas E. L., Bode P., Hoffman Y., 2004, *MNRAS*, 349, 595
- Lumb D. H., et al., 2004, *A&A*, 420, 853
- Majumdar S., Mohr J. J., 2003, *ApJ*, 585, 603
- Majumdar S., Mohr J. J., 2004, *ApJ*, 613, 41
- Mantz A., Allen S. W., Ebeling H., Rapetti D., 2008, *MNRAS*, 387, 1179
- Maughan B. J., 2007, *ApJ*, 668, 772
- Maughan B. J., Jones C., Forman W., Van Speybroeck L., 2008, *ApJS*, 174, 117

- Maughan B. J., Jones L. R., Ebeling H., Scharf C., 2006, *MNRAS*, 365, 509
- Mazzotta P., Rasia E., Moscardini L., Tormen G., 2004, *MNRAS*, 354, 10
- Melchiorri A., Bode P., Bahcall N. A., Silk J., 2003, *ApJ*, 586, L1
- Mewe R., Lemen J. R., van den Oord G., 1986, *A&A*, 65, 511
- Miller C. J., Romer A. K., Stanford S. A., Hilton M., Hosmer M., Merhtens N., 2006 Vol. 38 of *BAAS, The NOAO-XCS Survey Program*. pp 998–
- Morrison R., McCammon D., 1983, *ApJ*, 270, 119
- Nagai D., Kravtsov A. V., Vikhlinin A., 2007, *ApJ*, 668, 1
- Navarro J. F., Frenk C. S., White S. D. M., 1995, *MNRAS*, 275, 720
- Navarro J. F., Frenk C. S., White S. D. M., 1996, *ApJ*, 462, 563
- Navarro J. F., Frenk C. S., White S. D. M., 1997, *ApJ*, 490, 493
- Nichol R. C., Collins C. A., Guzzo L., Lumsden S. L., 1992, *MNRAS*, 255, 21P
- Nord B., Stanek R., Rasia E., Evrard A. E., 2008, *MNRAS*, 383, L10
- Novicki M. C., Sornig M., Henry J. P., 2002, *AJ*, 124, 2413
- Ota N., Kitayama T., Masai K., Mitsuda K., 2006, *ApJ*, 640, 673
- Ota N., Mitsuda K., 2004, *A&A*, 428, 757
- Oukbir J., Blanchard A., 1992, *A&A*, 262, L21
- Oukbir J., Blanchard A., 1997, *A&A*, 317, 1
- Pacaud F., et al., 2007, *MNRAS*, 382, 1289
- Padmanabhan N., et al., 2007, *MNRAS*, 378, 852
- Pierpaoli E., Scott D., White M., 2001, *MNRAS*, 325, 77
- Pierre M., Pacaud F., Melin J. B., 2008, *Astronomische Nachrichten*, 329, 143
- Pope A. C., et al., 2004, *ApJ*, 607, 655
- Predehl P., et al., 2006, in Turner M. J. L., Hasinger G., eds, *Space Telescopes and Instrumentation II: Ultraviolet to Gamma Ray*. Vol. 6266 of *Proceedings of the SPIE, eROSITA*
- Randall S. W., Sarazin C. L., Ricker P. M., 2002, *ApJ*, 577, 579
- Rapetti D., Allen S. W., Mantz A., 2008, *MNRAS*, pp 740–
- Rapetti D., Allen S. W., Weller J., 2005, *MNRAS*, 360, 555
- Rasia E., Mazzotta P., Borgani S., Moscardini L., Dolag K., Tormen G., Diaferio A., Murante G., 2005, *ApJ*, 618, L1
- Rasia E., Tormen G., Moscardini L., 2004, *MNRAS*, 351, 237
- Reed D., Gardner J., Quinn T., Stadel J., Fardal M., Lake G., Governato F., 2003, *MNRAS*, 346, 565
- Reed D. S., Bower R., Frenk C. S., Jenkins A., Theuns T., 2007, *MNRAS*, 374, 2
- Refregier A., Valtchanov I., Pierre M., 2002, *A&A*, 390, 1
- Reichart D. E., Nichol R. C., Castander F. J., Burke D. J., Romer A. K., Holden B. P., Collins C. A., Ulmer M. P., 1999, *ApJ*, 518, 521
- Reiprich T. H., Böhringer H., 2002, *ApJ*, 567, 716
- Romer A. K., Collins C. A., Böhringer H., Cruddace R. G., Ebeling H., MacGillivray H. G., Voges W., 1994, *Nat*, 372, 75
- Romer A. K., Viana P. T. P., Liddle A. R., Mann R. G., 2001, *ApJ*, 547, 594
- Rozo E., et al., 2007a, preprint (arXiv:astro-ph/0703571)
- Rozo E., Wechsler R. H., Koester B. P., Evrard A. E., McKay T. A., 2007b, preprint (arXiv:astro-ph/0703574)
- Sanderson A. J. R., Ponman T. J., O’Sullivan E., 2006, *MNRAS*, 372, 1496
- Schäfer B. M., Koyama K., 2008, *MNRAS*, pp 130–
- Seljak U., Zaldarriaga M., 1996, *ApJ*, 469, 437
- Shaw L. D., Weller J., Ostriker J. P., Bode P., 2006, *ApJ*, 646, 815
- Spergel D. N., et al., 2007, *ApJS*, 170, 377
- Stanek R., Evrard A. E., Böhringer H., Schuecker P., Nord B., 2006, *ApJ*, 648, 956
- Stanford S. A., et al., 2006, *ApJ*, 646, L13
- Szalay A. S., et al., 2003, *ApJ*, 591, 1
- Tang J.-Y., Weller J., Zablocki A., 2006, preprint (arXiv:astro-ph/0609028)
- Tegmark M., et al., 2004a, *PRD*, 69, 103501
- Tegmark M., et al., 2004b, *ApJ*, 606, 702
- Verde L., et al., 2003, *ApJS*, 148, 195
- Verde L., Haiman Z., Spergel D. N., 2002, *ApJ*, 581, 5
- Viana P. T. P., Kay S. T., Liddle A. R., Muanwong O., Thomas P. A., 2003, *MNRAS*, 346, 319
- Viana P. T. P., Liddle A. R., 1996, *MNRAS*, 281, 323
- Viana P. T. P., Liddle A. R., 1999, *MNRAS*, 303, 535
- Vikhlinin A., 2006, *ApJ*, 640, 710
- Vikhlinin A., et al., 2003, *ApJ*, 590, 15
- Vikhlinin A., Kravtsov A., Forman W., Jones C., Markevitch M., Murray S. S., Van Speybroeck L., 2006, *ApJ*, 640, 691
- Vikhlinin A., Van Speybroeck L., Markevitch M., Forman W. R., Grego L., 2002, *ApJ*, 578, L107
- Voit G. M., 2005a, *Advances in Space Research*, 36, 701
- Voit G. M., 2005b, *Rev. Mod. Phys.*, 77, 207
- Wang L., Steinhardt P. J., 1998, *ApJ*, 508, 483
- Wang S., Haiman Z., Hu W., Khoury J., May M., 2005, *PRL*, 95, 011302
- Wang S., Khoury J., Haiman Z., May M., 2004, *PRD*, 70, 123008
- Warren M. S., Abazajian K., Holz D. E., Teodoro L., 2006, *ApJ*, 646, 881
- Weller J., Battye R. A., Kneissl R., 2002, *PRL*, 88, 231301
- White M., 2002, *ApJS*, 143, 241
- Wittman D., Dell’Antonio I. P., Hughes J. P., Margoniner V. E., Tyson J. A., Cohen J. G., Norman D., 2006, *ApJ*, 643, 128
- Younger J. D., Haiman Z., Bryan G. L., Wang S., 2006, *ApJ*, 653, 27
- Zhang Y.-Y., Böhringer H., Finoguenov A., Ikebe Y., Matsushita K., Schuecker P., Guzzo L., Collins C. A., 2006, *A&A*, 456, 55

APPENDIX A: EQUATIONS**A1 Cluster counts***A1.1 Ideal measurements*

The expected number of clusters with temperatures between T_1 and T_2 at redshifts between z_1 and z_2 when measurements are assumed to be exact is given by

$$N_{\text{ideal}}(T_1, T_2, z_1, z_2) = \int_{z_1}^{z_2} \int_{T_1}^{T_2} n_{\text{ideal}}(T, z) dT dz \quad (\text{A1})$$

where n_{ideal} is the actual number density of clusters in temperature and redshift, given by the convolution of the mass function $n(M_t, z)$ with cluster scaling relations, their scatter (through $p(L_t, M_t)$), cosmic volume dV/dz and the survey selection function f_{sky} (including sky coverage):

$$n_{\text{ideal}}(T, z) = \int_{M_t} \int_{L_t} n(M_t, z) f_{\text{sky}}(L_t, T, z) p(L_t, M_t | L(T, z), M(T, z)) \frac{dV}{dz} dL_t dM_t. \quad (\text{A2})$$

The scaling-relation scatter probability distributions are assumed to be statistically independent,

$$p(L_t, M_t | L(T, z), M(T, z)) = p(L_t | L(T, z)) \times p(M_t | M(T, z)), \quad (\text{A3})$$

each having a log-normal form:

$$p(M_t | M(T, z), T, z) dM_t = p(T_t^M(M_t) | T, z) \frac{dM_t}{dT_t^M} dT_t^M = \frac{1}{\text{erf}(m_T/\sqrt{2})\sqrt{2\pi}\sigma_{\log T}} \exp\left[-\frac{1}{2} \frac{(\log_{10} T - \log_{10} T_t^M)^2}{\sigma_{\log T}^2}\right] \\ \times \Theta\left(m_T \sigma_{\log T} - |\log_{10} T - \log_{10} T_t^M|\right) \frac{dM_t}{dT_t^M} d\log_{10} T_t^M, \quad (\text{A4})$$

$$p(L_t | L(T, z)) dL_t = \frac{1}{\text{erf}(m_L/\sqrt{2})\sqrt{2\pi}\sigma_{\log L_X}} \exp\left[-\frac{1}{2} \frac{(\log_{10} L(T, z) - \log_{10} L_t)^2}{\sigma_{\log L_X}^2}\right] \\ \times \Theta\left(m_L \sigma_{\log L_X} - |\log_{10} L(T, z) - \log_{10} L_t|\right) d\log_{10} L_t. \quad (\text{A5})$$

The parameters m_T , m_L , $\sigma_{\log T}$ and $\sigma_{\log L}$ are described further in Sections 3.2 and 3.3 as well as Table 3.

A1.2 Measurement errors

When treating the case of measurement errors in T and z , we must distinguish observed and true temperature. The expected number of clusters between *observed* temperatures T_1 and T_2 , and redshifts z_1 and z_2 , is given by

$$N_{\text{obs}}(T_1, T_2, z_1, z_2) = \int_{z_1}^{z_2} \int_{T_1}^{T_2} \bar{n}(T, z) dT dz \quad (\text{A6})$$

where \bar{n} represents the cluster distribution marginalized over the probability distribution for measurements, i.e.

$$\bar{n}(T, z) = \int_{z_t} \int_{T_t} n_{\text{ideal}}(T_t, z_t) p(T, z | T_t, z_t) dT_t dz_t \\ = \int_{z_t} \int_{T_t} n_{\text{ideal}}(T_t, z_t) p\left(T \left[\frac{1+z_t}{1+z}\right] \middle| T_t, z_t\right) p(z | z_t) \left(\frac{1+z_t}{1+z}\right) dT_t dz_t, \quad (\text{A7})$$

Realistic T errors	Worst-case T errors
Eq. (A8)	Eq. (A8) with std. dev. $3 \times \sigma_T$

Table A1. Temperature error specifications.

Parameter	Description	Realistic z errors	Worst-case z errors
σ_0	Standard deviation at $z = 0$	0.05	0.10
c	Catastrophic standard deviation in units of σ_0	4	4
n	Min. deviation from mean in units of $c\sigma_0$ for catastrophic redshifts	1	1
f_{cat}	Fraction of catastrophic redshifts	0.05	0.10

Table A2. Redshift error specifications.

where z_t and T_t are true redshift and temperature, and in the last step the relation $T_{\text{obs}} = (1 + z_{\text{obs}})T_t/(1 + z_t)$ was used to go from observed to true temperature. The temperature and redshift measurement probability distributions are modelled by

$$p(T|T_t, z_t) dT = \frac{1}{\sqrt{\pi/2}(\sigma_T^- + \sigma_T^+)} \exp\left[-\frac{1}{2} \frac{(T - T_{\text{med}}(T_t, z_t))^2}{\sigma_T(T_t, z_t)^2}\right] dT \quad (\text{A8})$$

$$T_{\text{med}}(T_t, z_t)/T_t = \alpha_c + \alpha_T T_t + \alpha_z z_t + \alpha_{zz} z_t^2 + \alpha_{TT} T_t^2 + \alpha_{zT} z_t T_t$$

$$\sigma_T(T_t, z_t) = \begin{cases} \sigma_T^+ = T_t (\beta_c^+ + \beta_T^+ T_t + \beta_z^+ z_t + \beta_{zz}^+ z_t^2 + \beta_{TT}^+ T_t^2 + \beta_{zT}^+ z_t T_t), & T_t \geq T_{\text{med}}(T_t, z_t); \\ \sigma_T^- = T_t (\beta_c^- + \beta_T^- T_t + \beta_z^- z_t + \beta_{zz}^- z_t^2 + \beta_{TT}^- T_t^2 + \beta_{zT}^- z_t T_t), & \text{otherwise.} \end{cases}$$

where the α and β are determined from simulations (see Sect. 3.5)

$$p(z|z_t) dz = \frac{1}{N_z^{\text{rand}}(z_t)(1 - f_{\text{cat}}) + N_z^{\text{cata}}(z_t)f_{\text{cat}}} \left\{ (1 - f_{\text{cat}}) \exp\left[-\frac{1}{2} \frac{(z - z_t)^2}{\sigma_0^2(1 + z_t)^2}\right] + f_{\text{cat}} \exp\left[-\frac{1}{2} \frac{(z - z_t)^2}{c^2 \sigma_0^2(1 + z_t)^2}\right] \Theta(|z - z_t| - nc\sigma_0(1 + z_t)) \Theta(z) \right\} dz \quad (\text{A9})$$

$$N_z^{\text{rand}}(z_t) = \sqrt{\frac{\pi}{2}} \sigma_0(1 + z_t) \left[1 + \text{erf}\left(\frac{z_t}{\sqrt{2}\sigma_0(1 + z_t)}\right) \right]$$

$$N_z^{\text{cata}}(z_t) = \sqrt{2\pi} c \sigma_0(1 + z_t) \left(\text{erfc}\left(\frac{n}{\sqrt{2}}\right) - \frac{1}{2} \min\left[\text{erfc}\left(\frac{z_t}{\sqrt{2}c\sigma_0(1 + z_t)}\right), \text{erfc}\left(\frac{n}{\sqrt{2}}\right)\right] \right)$$

The temperature error assumptions made in this work are described further in Sect. 3.5 and summarized in Table A1. The redshift error assumptions for parameters f_{cat} , n , c and σ_0 are described further in Section 3.4 and Table A2. Note that the probability distributions of *true* temperatures and redshifts, the Bayesian “inverses” of the above, are weighted by the cluster distribution and given by

$$p(T_t|T, z_t) dT_t = \frac{p(T|T_t, z_t) n_{\text{ideal}}(T_t, z_t) dT_t}{\int p(T|T', z_t) n_{\text{ideal}}(T', z_t) dT'}, \quad (\text{A10})$$

$$p(z_t|T_t, z) dz_t = \frac{p(z|z_t) n_{\text{ideal}}(T_t, z_t) dz_t}{\int p(z|z') n_{\text{ideal}}(T_t, z') dz'}. \quad (\text{A11})$$

A2 Expected likelihood

In order to evaluate the expected constraints from a survey, one needs to consider some ensemble of possible outcomes and from that calculate, by ensemble averaging or otherwise (given a specification of ‘expected’), the expected constraints. We have chosen a type of smoothed Maximum Likelihood (ML) estimate, that captures the most likely shape and size of constraint contours but removes the offset associated with a traditional ML point estimate. In the following we show in detail that our expected constraints can be obtained accurately without averaging over many data realizations, but rather by using only an ‘average catalogue’.

Having an expression for the single-catalogue likelihood, we seek to estimate the expected constraints for the survey. We define this as the expected constraints for a set consisting of a certain fraction ε most likely catalogues. We start by setting up some formalism and prove our central theorem, and then go on to use this for our application.

Definition 1. Let $\{C_j\}$ denote a set of catalogues indexed by j . Let N be the number of bins of a catalogue. Let N_i or N_i^j be the observed number count for bin i , in catalogue j where superscript present. Let λ_i be the Poisson mean for bin i at which the likelihood is evaluated, and λ_i^* the same for the fiducial model used to generate the catalogues. Let $\delta_i^j \equiv N_i^j - \lambda_i^*$ measure the deviation of the observed number count from the fiducial-model mean.

Definition 2. Let the expected likelihood for the fraction ε most likely catalogues in a Poisson ensemble be given by

$$\langle \mathcal{L} \rangle_\varepsilon \equiv \prod_i e^{-\lambda_i} \left\langle \prod_i \left[\frac{\lambda_i^{N_i}}{N_i!} \right] \right\rangle_\varepsilon, \quad (\text{A12})$$

where the product runs over the N bins in a catalogue, and $\langle \cdot \rangle_\varepsilon$ denotes a Poisson ensemble average restricted to catalogues C_j such that $\sum_j P(C_j) \Theta(P(C_j) - P_\varepsilon) = \varepsilon$ (with Θ the Heaviside step function). This expression also defines the probability threshold P_ε .

Corollary 1. It follows from the above definition and the Poisson distribution that

$$\langle \mathcal{L} \rangle_\varepsilon = \prod_i e^{-\lambda_i} \sum_j \frac{P(C_j)}{\varepsilon} \prod_i \left[\frac{\lambda_i^{N_i^j}}{N_i^{j!}} \right] \Theta(P(C_j) - P_\varepsilon) = e^{-\sum_i (\lambda_i + \lambda_i^*)} \frac{1}{\varepsilon} \sum_j \prod_i \frac{(\lambda_i \lambda_i^*)^{\lambda_i^* + \delta_i^j}}{[(\lambda_i^* + \delta_i^j)!]^2} \Theta(P(C_j) - P_\varepsilon). \quad (\text{A13})$$

Definition 3. Let

$$\mathcal{C}_\pm \equiv \left\{ \{\delta_i\}_{i=1}^N \mid \delta_i \in \{\lceil \lambda_i^* \rceil - \lambda_i^*, \lfloor \lambda_i^* \rfloor - \lambda_i^*\} \forall i \right\}, \quad (\text{A14})$$

the set of catalogues consisting of the 2^N catalogues between the most likely catalogue (for which $\delta_i = \lfloor \lambda_i^* \rfloor - \lambda_i^* \forall i$) to the catalogue with probability P_ε (for which $\delta_i = \lceil \lambda_i^* \rceil - \lambda_i^* \forall i$). Here, $\lceil \cdot \rceil$ and $\lfloor \cdot \rfloor$ are the ceiling and floor operators respectively.

Remark 1. The choice of this set of catalogues will be convenient and is suitable to define a smoothed ML estimate.

We now come to the central theorem:

Theorem 1. For the catalogue set \mathcal{C}_\pm ,

$$\langle \mathcal{L} \rangle_\varepsilon = \sum_i \left(\lceil \lambda_i^* \rceil - \frac{1}{2} \right) \ln \lambda_i - \lambda_i + \mathcal{O}(\delta^3) + \text{const.} \quad (\text{A15})$$

Proof. The probability level ε for the catalogue set \mathcal{C}_\pm can be estimated through

$$\prod_i \frac{(\lambda_i^*)^{\lceil \lambda_i^* \rceil}}{\lceil \lambda_i^* \rceil!} \leq \frac{\varepsilon}{2^N e^{-\sum_i \lambda_i^*}} \leq \prod_i \frac{(\lambda_i^*)^{\lfloor \lambda_i^* \rfloor}}{\lfloor \lambda_i^* \rfloor!}. \quad (\text{A16})$$

We approximate

$$\varepsilon \approx 2^N e^{-\sum_i \lambda_i^*} \prod_i \frac{(\lambda_i^*)^{\lambda_i^*}}{\Gamma(1 + \lambda_i^*)}, \quad (\text{A17})$$

where we have used the gamma function as a continuation of the factorial, effectively extending the Poisson distribution to the gamma distribution for non-integer values of N_i , something we will use throughout. We can now write

$$\langle \mathcal{L} \rangle_\varepsilon = 2^{-N} e^{-\sum_i \lambda_i} \sum_j \prod_i \frac{(\lambda_i)^{\lambda_i^* + \delta_i^j} (\lambda_i^*)^{\delta_i^j}}{[(\lambda_i^* + \delta_i^j)!]^2} \Gamma(1 + \lambda_i^*), \quad (\text{A18})$$

where the catalogues (indexed by j) are now restricted to those in \mathcal{C}_\pm . To proceed, we first take the logarithm of the likelihood to separate out the catalogue-set-dependent normalization, which is of no consequence for our discussion. We can thus write

$$\ln \langle \mathcal{L} \rangle_\varepsilon = -N \ln 2 + \sum_i [-\lambda_i + \lambda_i^* \ln \lambda_i + \ln \Gamma(1 + \lambda_i^*)] + \ln \hat{\Sigma}, \quad (\text{A19})$$

where we have defined

$$\hat{\Sigma} \equiv \sum_j \prod_i \frac{(\lambda_i \lambda_i^*)^{\delta_i^j}}{[(\lambda_i^* + \delta_i^j)!]^2}. \quad (\text{A20})$$

Taylor expanding in δ_i^j (since $|\delta_i^j| < 1$ for our catalogues) we find

$$\begin{aligned} \ln \langle \mathcal{L} \rangle_\varepsilon &= -N \ln 2 + \sum_i [\lambda_i^* \ln \lambda_i - \lambda_i + \ln \Gamma(1 + \lambda_i^*)] + \ln \hat{\Sigma} \Big|_{\delta=0} + \sum_{i,j} \left(\frac{1}{\hat{\Sigma}} \frac{d\hat{\Sigma}}{d\delta_i^j} \right) \Big|_{\delta=0} \delta_i^j + \\ &\quad \frac{1}{2} \sum_{i,j,k,l} \left[\frac{1}{\hat{\Sigma}} \left(\frac{d^2 \hat{\Sigma}}{d\delta_i^j d\delta_k^l} - \frac{1}{\hat{\Sigma}} \frac{d\hat{\Sigma}}{d\delta_i^j} \frac{d\hat{\Sigma}}{d\delta_k^l} \right) \right] \Big|_{\delta=0} \delta_i^j \delta_k^l + \mathcal{O}(\delta^3), \end{aligned} \quad (\text{A21})$$

where “ $\delta = 0$ ” denotes $\delta_i^j = 0 \forall i, j$. Inserting $\hat{\Sigma}$ and the derivatives

$$\frac{d\hat{\Sigma}}{d\delta_i^j} = \ell(\lambda_i, \lambda_i^*) \prod_k \frac{(\lambda_k \lambda_k^*)^{\delta_k^j}}{[(\lambda_k^* + \delta_k^j)!]^2}, \quad (\text{A22})$$

$$\frac{d^2 \hat{\Sigma}}{d\delta_i^j d\delta_k^l} = \ell(\lambda_i, \lambda_i^*) \ell(\lambda_k, \lambda_k^*) \prod_m \frac{(\lambda_m \lambda_m^*)^{\delta_m^j}}{[(\lambda_m^* + \delta_m^j)!]^2} \tilde{\delta}_{jl}, \quad (\text{A23})$$

where $\ell(\lambda, \lambda^*) \equiv \ln(\lambda \lambda^*) - 2\Psi(1 + \lambda^*)$ (the digamma function Ψ coming from the factorial as gamma function), we obtain

$$\begin{aligned} \ln \langle \mathcal{L} \rangle_\varepsilon &= \sum_i (\lambda_i^* \ln \lambda_i - \lambda_i) + \sum_i \ell(\lambda_i, \lambda_i^*) 2^{-N} \sum_j \delta_i^j + \\ &\quad \frac{1}{2} \sum_{i,j,k,l} 2^{-N} \left[\ell(\lambda_i, \lambda_i^*) \ell(\lambda_k, \lambda_k^*) \tilde{\delta}_{jl} - 2^{-N} \ell(\lambda_i, \lambda_i^*) \ell(\lambda_k, \lambda_k^*) \right] \delta_i^j \delta_k^l + \mathcal{O}(\delta^3) \end{aligned} \quad (\text{A24})$$

$$\begin{aligned} &= \sum_i (\lambda_i^* \ln \lambda_i - \lambda_i) + \sum_i \ell(\lambda_i, \lambda_i^*) 2^{-N} \sum_j \delta_i^j + \\ &\quad \frac{1}{2} \sum_{i,k} \ell(\lambda_i, \lambda_i^*) \ell(\lambda_k, \lambda_k^*) \left[2^{-N} \sum_j \delta_i^j \delta_k^j - 2^{-2N} \sum_{j,l} \delta_i^j \delta_k^l \right] + \mathcal{O}(\delta^3), \end{aligned} \quad (\text{A25})$$

where $\tilde{\delta}_{ij}$ is the Kronecker delta. We can evaluate the δ -sums using our knowledge of the set of catalogues \mathcal{C}_\pm :

$$\sum_j \delta_i^j = 2^{N-1} (\lceil \lambda_i^* \rceil + \lfloor \lambda_i^* \rfloor - 2\lambda_i^*) = 2^N \left(\Delta_i^* - \frac{1}{2} \right), \quad (\text{A26})$$

$$\sum_{j,l} \delta_i^j \delta_k^l = 2^{2N} \left(\Delta_i^* - \frac{1}{2} \right) \left(\Delta_k^* - \frac{1}{2} \right) = 2^{2N} \left[\Delta_i^* \Delta_k^* - \frac{1}{2} (\Delta_i^* + \Delta_k^*) + \frac{1}{4} \right], \quad (\text{A27})$$

$$\sum_j \delta_i^j \delta_k^j = \frac{2^N}{4} [\Delta_i^* \Delta_k^* + \Delta_i^* (\Delta_k^* - 1) + (\Delta_i^* - 1) \Delta_k^* + (\Delta_i^* - 1) (\Delta_k^* - 1)] = 2^N \left[\Delta_i^* \Delta_k^* - \frac{1}{2} (\Delta_i^* + \Delta_k^*) + \frac{1}{4} \right], \quad (\text{A28})$$

where we have defined $\Delta_i^* \equiv \lceil \lambda_i^* \rceil - \lambda_i^*$ and excluded the possibility that $\lceil \lambda_k^* \rceil = \lfloor \lambda_k^* \rfloor = \lambda_k^*$. Inserting (A27) and (A28) in (A25) we find that the second-order term is zero due to cancellation between its two constituent terms. Hence, also inserting (A26), we finally arrive at

$$\ln \langle \mathcal{L} \rangle_\varepsilon = \sum_i \left[\lambda_i^* \ln \lambda_i - \lambda_i + \ell(\lambda_i, \lambda_i^*) \left(\Delta_i^* - \frac{1}{2} \right) \right] + \mathcal{O}(\delta^3) \quad (\text{A29})$$

$$= \sum_i \left[\left(\lceil \lambda_i^* \rceil - \frac{1}{2} \right) \ln \lambda_i - \lambda_i + \left(\Delta_i^* - \frac{1}{2} \right) (\ln \lambda_i^* - 2\Psi(1 + \lambda_i^*)) \right] + \mathcal{O}(\delta^3). \quad (\text{A30})$$

□

The theorem states that a good approximation to $\langle \mathcal{L} \rangle_\varepsilon$ is given by using $N_i = \lceil \lambda_i^* \rceil - 1/2$ in a single-catalogue likelihood \mathcal{L} . This expression, however, does give rise to an offset in the best-fitting values away from the true means, associated with shot noise. As we are using the catalogue construction as a way of defining a meaningful expected likelihood which is not just an arbitrary point estimate, we are not really interested in this offset (and would like to separate it from sources of bias); rather the variance is what concerns us. Therefore, we propose using the very similar expression

$$\langle \ln \mathcal{L} \rangle = \sum_i (\lambda_i^* \ln \lambda_i - \lambda_i) + \text{const.} \quad (\text{A31})$$

The best-fitting values for λ_i of this expression are equal to the true means λ_i^* . However, how do the standard deviations compare? The standard deviations are given by

$$\sigma_{\varepsilon,i} = \sqrt{\lceil \lambda_i^* \rceil - 1/2}, \quad \sigma_{\text{mean},i} = \sqrt{\lambda_i^*}, \quad (\text{A32})$$

where $\sigma_{\varepsilon,i}$ is the standard deviation of equation (A30) and $\sigma_{\text{mean},i}$ the standard deviation of equation (A31). Upper and lower limits for their ratio can then be given as

$$\frac{1}{\sqrt{1 + 1/2\lambda_i^*}} < \frac{\sigma_{\text{mean},i}}{\sigma_{\varepsilon,i}} < \frac{1}{\sqrt{1 - 1/2\lambda_i^*}}. \quad (\text{A33})$$

It is clear that for $\lambda_i^* < 1$ the relative error will become large as λ_i^* decreases. Again, this is due to shot noise. One could always make bins large enough that at least a few elements fall in each bin, ensuring only moderate relative errors in the standard deviations. Such a binning might however not be optimal or even close to, and thus reflect the underlying distribution poorly. It appears that no general conclusion can be drawn here. However, if we specify a dependence $\lambda_i = \lambda_i^* (\theta/\theta^*)^{a_i}$ for the λ_i 's on some parameter θ , as is typically the case and certainly here, we can write the following:

$$\langle \ln \mathcal{L} \rangle = \sum_i (\lambda_i^* \ln \lambda_i - \lambda_i) + \text{const.} = \ln \theta \sum_i a_i \lambda_i^* - \sum_i \lambda_i^* \left(\frac{\theta}{\theta^*} \right)^{a_i} + \text{const.} \quad (\text{A34})$$

$$\ln \langle \mathcal{L} \rangle_\varepsilon = \sum_i \left[\left(\lceil \lambda_i^* \rceil - \frac{1}{2} \right) \ln \lambda_i - \lambda_i \right] + \text{const.} = \ln \theta \sum_i a_i \left(\lceil \lambda_i^* \rceil - \frac{1}{2} \right) - \sum_i \lambda_i^* \left(\frac{\theta}{\theta^*} \right)^{a_i} + \text{const.} \quad (\text{A35})$$

Clearly, the only difference between $\ln \langle \mathcal{L} \rangle_\varepsilon$ and $\langle \ln \mathcal{L} \rangle$ comes from the difference in the first sum. Naively, we would not expect this to differ

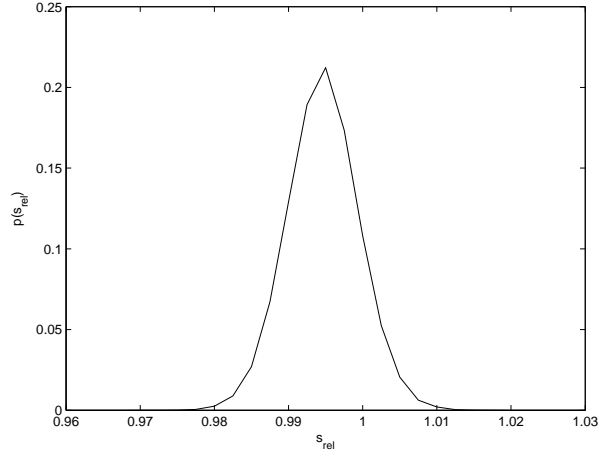


Figure A1. The probability density function for s_{rel} for a typical XCS catalogue with $a_i \in U(-5, 5)$.

much between the two cases, particularly for a binning that represents the distribution well. What would be the expected value? Consider the following quantity:

$$s_{\text{rel}} \equiv \frac{\sum_i a_i \lambda_i^*}{\sum_i a_i (\lceil \lambda_i^* \rceil - \frac{1}{2})} = \frac{\sum_i a_i \lambda_i^*}{\sum_i a_i (\lambda_i^* + (\lceil \lambda_i^* \rceil - \lambda_i^*) - \frac{1}{2})}. \quad (\text{A36})$$

One would generally expect that $(\lceil \lambda^* \rceil - \lambda^*) \in U(0, 1)$ or at least a similarly symmetric distribution across the bins, so that $\langle \lceil \lambda^* \rceil - \lambda^* \rangle = 1/2$. We thus expect

$$\langle s_{\text{rel}} \rangle = \frac{\sum_i a_i \lambda_i^*}{\langle \sum_i a_i (\lceil \lambda_i^* \rceil - \frac{1}{2}) \rangle} = \frac{\sum_i a_i \lambda_i^*}{\sum_i a_i \lambda_i^*} = 1. \quad (\text{A37})$$

For typical XCS catalogues, even if we assign uncorrelated random exponents a_i , the probability distribution for s_{rel} is quite generally very sharply peaked at or close to $s_{\text{rel}} = 1$. An example is shown in Fig. A1, for which $a_i \in U(-5, 5)$. Furthermore, finding typical a_i 's for the various XCS models, we find that $s_{\text{rel}} = 1 + \mathcal{O}(10^{-2})$.

In conclusion, the likelihood $\langle \ln \mathcal{L} \rangle$ of the average catalogue is a good approximation to the average likelihood $\ln \langle \mathcal{L} \rangle_\varepsilon$ of our set of catalogues \mathcal{C}_\pm , and can also generally be expected to be a good approximation in other similar applications. We have confirmed this by explicitly comparing to the likelihoods for a Poisson sample of catalogues, as shown in Fig. 6 in the main text.

This paper has been typeset from a \LaTeX file prepared by the author.